
KAIROS: Toward Adaptive and Parameter-Efficient Time Series Foundation Models

Kun Feng^{*1} Shaocheng Lan^{*1} Yuchen Fang^{*2} Wenchao He¹ Lintao Ma² Xingyu Lu² Kan Ren¹

Abstract

Inherent temporal heterogeneity, such as varying sampling densities and periodic structures, has posed substantial challenges in zero-shot generalization for Time Series Foundation Models (TSFMs). Existing TSFMs predominantly rely on massive parameterization to absorb such heterogeneity, as their static tokenization and positional encoding schemes entangle diverse temporal patterns into a fixed representation space, encouraging memorization rather than adaptation. To address this limitation, we propose KAIROS, a flexible and parameter-efficient TSFM that decouples temporal heterogeneity from model capacity through a novel tokenization perspective. KAIROS introduces a dynamic patching tokenizer and a mixture-of-size encoding that adapt observational granularity to local information density, enabling fine-grained temporal abstraction without increasing model width or depth. In addition, we design a multi-granularity positional embedding based on dynamic rotary encodings, which conditions on instance-level spectral features and temporal structure induced by dynamic patching tokenization, allowing robust modeling of diverse temporal dependencies. Trained on a novel Predictability-Stratified Time-Series (PreSTS) corpus, KAIROS achieves superior zero-shot performance with substantially fewer parameters on two mainstream benchmarks, GIFT-Eval and Time-Series-Library. The project page is at <https://foundation-model-research.github.io/Kairos>.

1. Introduction

Time series forecasting is a core component of many real-world applications (Box et al., 2015; Wang et al., 2024b). Although time series data are ubiquitous, many individual datasets suffer from scarcity, making it difficult to train models independently, particularly for deep neural networks that require large amounts of data. This challenge has long motivated the development of few-shot and zero-shot forecasting methods (Oreshkin et al., 2020). More recently, inspired by the success of large-scale foundation models (Achiam et al., 2023; Kirillov et al., 2023), researchers have turned to building Time Series Foundation Models (TSFMs) for forecasting. These models leverage vast and diverse time series corpora to acquire strong generalization capabilities, showing promising results across various downstream tasks (Ansari et al., 2024; Woo et al., 2024; Shi et al., 2024).

Despite this progress, a key limitation persists: current TSFMs rely on non-adaptive processing pipelines that fail to reflect the dynamic and heterogeneous nature of time series, severely compromising their parameter efficiency. As shown in Figure 1(b)(c), the statistical information density (details in Appendix G) varies not only across datasets but also across segments within the same series. By applying rigid architectures (exemplified in Figure 1(d)) to this inherently heterogeneous data, models are forced to use massive parameters to memorize specific patterns rather than acquiring adaptive, generalizable rules. Unfortunately, this strategy diminishes the overall utility of the model’s capacity, rendering it less effective for real-world deployment.

This deficiency manifests primarily in two fundamental aspects of model design: (i) *Representation learning*: TSFMs have yet to adopt dynamic *tokenization strategies* analogous to those in Large Language Models (LLMs). While LLMs utilize subword tokenization (Gage, 1994) to efficiently compress semantic units of varying lengths, TSFMs predominantly persist with static patching, whether through point-wise tokenization (Ansari et al., 2024; Shi et al., 2024) or fixed-size patches (Das et al., 2024). By coupling token generation to fixed time intervals rather than information content, these approaches forcibly compress diverse temporal variations into a rigid representation space. Consequently, the model wastes computational capacity on

^{*}Equal contribution ¹School of Information Science and Technology, ShanghaiTech University, Shanghai, China ²Ant Group, Shanghai, China. Correspondence to: Kan Ren <renkan@shanghaitech.edu.cn>.

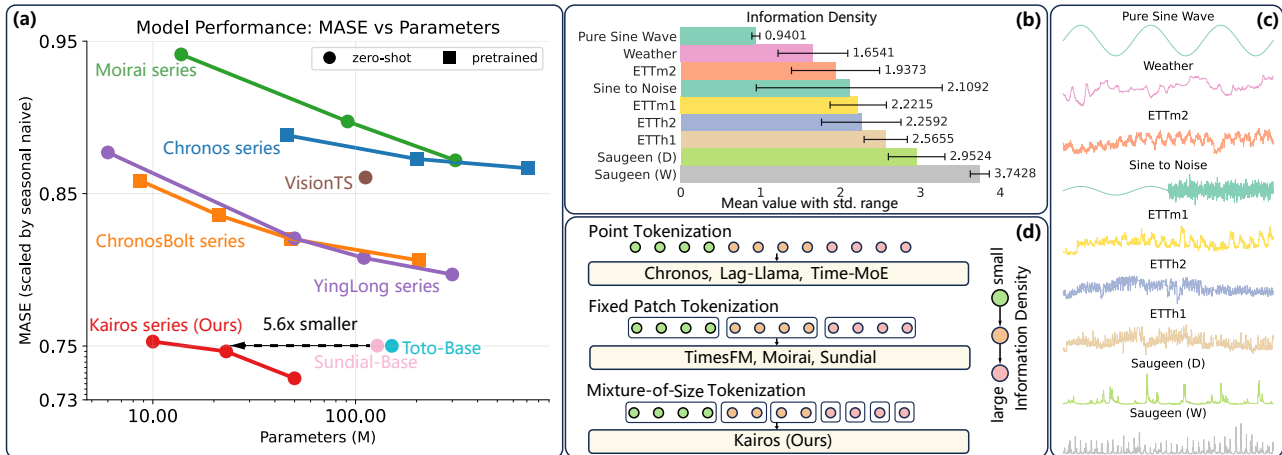


Figure 1. (a) Comparison on the GIFT-Eval benchmark (Aksu et al., 2024) demonstrates that our KAIROS achieves superior zero-shot forecasting performance (lower normalized MASE) while requiring significantly fewer parameters than existing TSFMs. (b) (c) Significant variation exists in information density (i.e., signal complexity) across and within different time series datasets. (d) Existing TSFMs primarily use tokenization methods like point-wise or fixed-size patching, while our KAIROS uses Mixture-of-Size Tokenization to dynamically adapt to information density, enabling the learning of generalizable rules rather than memorization.

low-information segments while struggling to capture high-frequency details within the same fixed budget, leading to significant parameter inefficiency. (ii) *Temporal dependency modeling*: Conventional *positional encodings* in TSFMs impose a unified temporal scale across sequences, neglecting differences in periodicity, trend and seasonality. As a result, existing TSFMs like (Liu et al., 2025) struggle to adapt to heterogeneous domains, for example, power consumption data measured hourly versus retail sales data measured daily, each exhibiting distinct temporal dynamics, as we empirically validate in Section 4.3. Consequently, the model requires a deeper, more complex architecture to compensate for this misalignment, further exacerbating parameter inefficiency and hindering practical utility.

To address these limitations, we propose KAIROS, a parameter-efficient model comprising a Mixture-of-Size Encoder, a Heterogeneity-Aware Transformer, and a Multi-Patch Decoder. KAIROS addresses time series heterogeneity through two primary mechanisms: (i) For intra-patch representation learning, the Mixture-of-Size Encoder adaptively models time series at multiple granularities based on local characteristics. Inspired by null experts in Mixture-of-Experts (Zeng et al., 2024; Jin et al., 2024), we introduce null patch sizes to dynamically adjust the number of active granularities. This approach moves beyond static tokenization strategies, enabling more expressive modeling of nuanced, time-varying dynamics. (ii) For inter-patch dependency modeling, we enhance the Transformer with Dynamic Rotary Position Embedding (DRoPE). Unlike standard RoPE (Su et al., 2024), which represents positional information with a fixed temporal scale, DRoPE modulates temporal scales using spectral features and granularity to

generate instance-specific positional encodings. Flexible intra-patch and inter-patch modeling enable KAIROS to effectively characterize heterogeneous time series with a substantially reduced parameter count (see Figure 1(a)). Additionally, the Multi-Patch Decoder uses learnable tokens to predict future patches in parallel, which mitigates cumulative errors in autoregressive generation and offers greater flexibility for variable-length prediction horizons.

To further enhance training, we construct the Predictability-Stratified Time Series (PreSTS) corpus, a large-scale and diverse pretraining dataset curated through a targeted sampling strategy. By prioritizing more predictable sequences while maintaining broad coverage, PreSTS provides high-quality supervision that supports efficient model scaling. As demonstrated by the results on the GIFT-Eval benchmark (Aksu et al., 2024) in Figure 1(a), these combined innovations allow our KAIROS to achieve superior performance while using fewer parameters. This strong performance is consistently observed on Time-Series-Library (TSLib) (Wang et al., 2024b) benchmarks as well.

In summary, our main contributions are as follows: (i) We present KAIROS, a parameter-efficient time series foundation model designed to handle the dynamic and heterogeneous nature of time series data. (ii) We introduce three key architectural innovations: the Mixture-of-Size Encoder for adaptive multi-granularity tokenization, DRoPE for instance-specific temporal calibration, and the Multi-Patch Decoder for flexible and efficient parallel forecasting. (iii) Extensive empirical evaluations on the GIFT-Eval and Time-Series-Library benchmarks confirm the efficacy of KAIROS, highlighting its superior zero-shot forecasting performance.

2. Related Work

Time Series Foundation Models (TSFMs). Inspired by the strong generalization of Large Language Models (LLMs), researchers have devoted increasing attention to TSFMs. Existing approaches typically involve adapting LLMs to time series (Gruver et al., 2023), training scalable Transformers on large corpora (Ansari et al., 2024; Das et al., 2024; Woo et al., 2024; Cohen et al., 2025; Liu et al., 2025), or exploring alternative architectures, including non-Transformer models (Auer et al., 2025; Graf et al., 2025) and lightweight Multi-Layer Perceptrons (Ekambaram et al., 2024). However, these models often apply fixed tokenization strategies and position embedding to time series from diverse domains with distinct characteristics, limiting their cross-domain generalization. KAIROS, in contrast, employs a dynamic patching tokenizer and instance-adaptive, granularity-aware position embedding to enhance its generalizability for diverse time series data.

Time Series Tokenization. Transformer-based models require converting raw data into discrete or continuous tokens (Sennrich et al., 2016; Agarwal et al., 2025). Current strategies generally fall into two static paradigms: (i) Fixed-size: The dominant paradigm relies on a uniform patch size across the sequence. This ranges from fine-grained point-wise tokenization (Ansari et al., 2024; Rasul et al., 2023; Shi et al., 2024) to coarser uni-size patching (Nie et al., 2023), which has been adopted by recent foundation models (Woo et al., 2024; Liu et al., 2025). While the latter improves upon the computational inefficiency of point-wise methods, both remain rigid. (ii) Multi-size: To capture broader temporal dynamics, models like Pathformer (Chen et al., 2024) and TTM (Ekambaram et al., 2024) incorporate multiple predefined patch sizes. However, these scales are applied statically, rather than adapting to the time series instance. All the above approaches partition sequences based on fixed time intervals rather than local information. This rigidity forces the model to allocate equal parameters to segments of varying complexity. This imbalance inevitably leads to suboptimal parameter efficiency and limited generalization. In contrast, KAIROS employs a mixture-of-size strategy. By allocating fewer tokens to simple patterns and more to complex regions, KAIROS significantly enhances parameter efficiency while maintaining robust generalization.

Position Embedding. Due to the position-unaware characteristic of self-attention mechanism, Transformers (Vaswani et al., 2017) rely on position embeddings (PEs) to model temporal information. However, most TSFMs adopt existing designs for PE in Natural Language Processing (NLP) domains (Das et al., 2024; Shi et al., 2024), which typically emphasize long-term decay through methods like sinusoidal calculations or by suppressing long-range positional information (Vaswani et al., 2017; Su et al., 2024). By imposing

a uniform temporal scale, these PEs struggle to model the heterogeneous temporal relationships of time series. Existing adaptive PE methods in NLP (Zheng et al., 2024; Lin et al., 2024) are also insufficient, as they target context extrapolation rather than the complex temporal structures of time series. Therefore, ElasTST (Zhang et al., 2024) proposed a tunable RoPE to better adapt to time series data. However, its adaptation uses per-dataset training rather than dynamic adjustment. To address this limitation, we propose to dynamically modulate PE tailored to the intrinsic characteristics of each input time series, enhancing the parameter efficiency and overall performance of TSFMs.

3. Methodology

3.1. Overall Framework

We formulate our task as learning a time series forecasting function $f_\phi : \mathbb{R}^T \rightarrow \mathbb{R}^H$ parameterized by ϕ . Given historical time series $\mathbf{X} \in \mathbb{R}^T$, time series forecasting is to predict the future horizon $\mathbf{Y} \in \mathbb{R}^H$. The learning objective is to minimize the discrepancy between the ground truth \mathbf{Y} and the prediction $\hat{\mathbf{Y}} = f_\phi(\mathbf{X})$. We detail it in Appendix D.1.2.

The architecture of KAIROS, shown in Figure 2, consists of three components. First, the input time series is tokenized by the Mixture-of-Size Encoder to extract multi-granularity local representations via dynamic granularity selection. These embeddings are then processed by a Heterogeneity-Aware Transformer equipped with Dynamic Rotary Position Embedding (DRoPE), a granularity-aware positional encoding that performs instance-wise modulation and adapts to dynamic patching tokenization. Finally, the Multi-Patch Decoder generates forecasts by predicting multiple future patches in parallel, mitigating cumulative errors. The details of these components are presented in the following sections.

3.2. Mixture-of-Size Encoder

Prior to the Heterogeneity-Aware Transformer (Section 3.3), the Mixture-of-Size Encoder adaptively tokenizes the raw time series \mathbf{X} through a three-stage process. First, the series is partitioned into fixed-size *segments*, where a router dynamically selects optimal temporal granularities *for each segment*. Next, for each activated granularity, the segment is simultaneously patchified and projected into the latent space by the expert network corresponding to that granularity. Finally, these multi-granularity embeddings are fused into a unified token sequence representing the input series.

Notably, the Mixture-of-Size Encoder is both *sparse* and *dynamic*. A gating mechanism equipped with null experts (described below) adaptively selects relevant granularities *for each segment*, enabling sparse expert activation and segment-specific granularity adaptation.

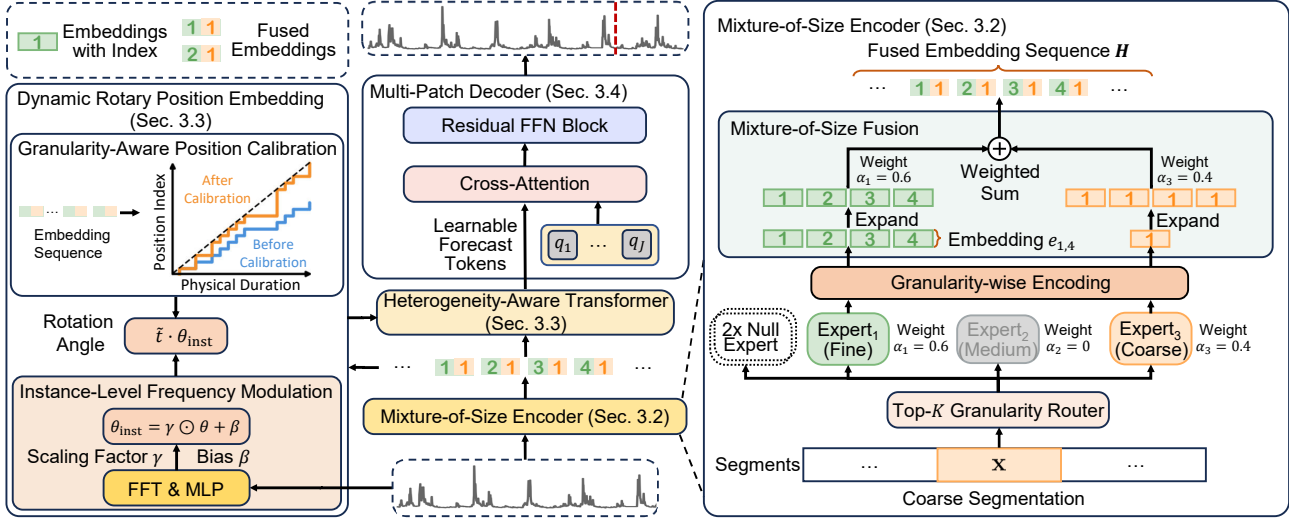


Figure 2. The architecture of KAIROS, which includes (i) The Mixture-of-Size Encoder (right) adaptively tokenizes the input series by routing segments to optimal granularity experts and fusing their embeddings into a unified sequence H . (ii) The Heterogeneity-Aware Transformer (middle) processes these tokens using Dynamic Rotary Position Embedding (DRoPE) (left), which modulates frequencies based on instance-level spectral features and calibrates positions to account for varying patch sizes. (iii) The Multi-Patch Decoder (top-middle) employs learnable forecast tokens to predict multiple future patches in parallel via cross-attention.

Coarse Segmentation. As shown in Figure 1(b) in Section 1 where time series exhibits inherent temporal heterogeneity, we first apply coarse segmentation to the input time series \mathbf{X} and process each segment independently in subsequent tokenization and encoding stages. Specifically, \mathbf{X} is partitioned into a sequence of non-overlapping coarse segments $\mathbf{X} = [\mathbf{x}_1, \dots, \mathbf{x}_N]$, where each segment \mathbf{x} has a fixed length P and the total number of segments is $N = \lceil T/P \rceil$. In the following, we operate within each segment \mathbf{x} and therefore omit the segment index for notational simplicity.

Granularity. For a given time series segment \mathbf{x} , we adopt a multi-granularity modeling perspective. *Granularity* refers to the temporal resolution at which the segment is tokenized and encoded, as defined below.

Definition 3.1 (Granularity Level). A *granularity level* $i \in \{1, \dots, G\}$ is defined by a specific patch size P_i and its corresponding encoding network π_i , under which the time series segment \mathbf{x} is patchified and mapped into a latent representation.

Intuitively, finer granularity levels capture high-frequency local variations, while coarser granularity levels emphasize low-frequency global trends. At each granularity level i , the patchification and embedding operations described below are applied independently and in parallel, producing representations that characterize the segment at the corresponding temporal resolution.

Step 1: Top- K Granularity Routing. Applying encoding at an appropriate granularity level for each time se-

ries segment is non-trivial due to the inherent temporal heterogeneity of time series data. To address this challenge, we introduce a dynamic routing mechanism equipped with a lightweight *router* that adaptively selects an optimal subset of granularity levels for subsequent encoding of a given segment. Inspired by the Mixture-of-Experts (MoE) paradigm (Jacobs et al., 1991; Shazeer et al., 2017), we instantiate G granularity-specific experts, each corresponding to a distinct granularity level, together with $Z \in \{1, \dots, K - 1\}$ null experts that perform no computation. The inclusion of null experts allows the model to implicitly skip encoding at certain granularities, enabling adaptive control over the *effective number of active granularities for each input segment*. The routing weights are computed via a learnable scoring function. Specifically, for each expert $i \in \{1, \dots, G + Z\}$, an affinity score is first computed as $s_i = \mathbf{w}_i^\top \mathbf{x}$, which is then normalized with a bias-corrected softmax $\tilde{s}_i = (\exp(s_i + \mathbf{b}_i)) / (\sum_{j=1}^{G+Z} \exp(s_j + \mathbf{b}_j))$, where \mathbf{w}_i denotes learnable parameters and \mathbf{b}_i is a bias term introduced for auxiliary-loss-free load balancing (Liu et al., 2024a) (details in Appendix D.3.1). The router thus produces a set of active granularity indices $\mathcal{I}_{\text{valid}} = \text{argtop-}K_{i \in [G+Z]} \tilde{s}_i \cap \{1, \dots, G\}$. That is, only the Top- K granularity experts are activated, while null experts contribute no computation even when selected. By selectively activating granularity experts and allowing null experts to absorb routing probability mass, KAIROS dynamically adapts the effective granularity resolution for *each time series segment* according to its local information, while maintaining a sparse and parameter-efficient architecture.

Step 2: Granularity-wise Encoding. For each selectively activated granularity expert at level i , we apply the corresponding patching and embedding operations. Specifically, a given time series *segment* \mathbf{x} is re-partitioned into a sequence of patches at granularity i :

$$[\mathbf{p}_{i,1}, \dots, \mathbf{p}_{i,M_i}] = \text{Patchify}(\mathbf{x}, i) \in \mathbb{R}^{M_i \times P_i}, \quad (1)$$

where P_i denotes the patch size at granularity i , and $M_i = \lceil P/P_i \rceil$ is the resulting number of patches obtained via non-overlapping segmentation, with zero-padding applied when necessary. Each patch is then projected into the latent space to obtain an embedding sequence $\mathbf{E}_i = [e_{i,1}, \dots, e_{i,M_i}]$:

$$e_{i,m} = \pi_i(\mathbf{p}_{i,m}) \in \mathbb{R}^{D_h}, m \in [1, M_i]. \quad (2)$$

where π_i denotes a granularity-specific projection function, implemented as a two-layer multilayer perceptron (MLP).

Step 3: Mixture-of-Size Fusion. In the final encoder stage, we fuse the embeddings produced by the activated granularity experts into a unified token sequence, serving as the input to the Heterogeneity-Aware Transformer. First, for a time-series segment \mathbf{x} , we align all granularity-specific embeddings \mathbf{E}_i to the finest activated resolution $P_{\min} = \min\{P_i \mid i \in \mathcal{I}_{\text{valid}}\}$, yielding a target sequence length $M = \lceil P/P_{\min} \rceil$. This alignment is crucial to eliminate representation bias arising from unequal sequence lengths induced by different patch sizes across granularities. To enable efficient alignment, we design the patch sizes to be nested, i.e., P_{i+1} is divisible by P_i . Under this constraint, each embedding sequence $\mathbf{E}_i \in \mathbb{R}^{M_i \times D_h}$ can be deterministically expanded to the target resolution via repetition (details and an example in Appendix D.3.2): $\tilde{\mathbf{E}}_i = \text{Expand}(\mathbf{E}_i) \in \mathbb{R}^{M \times D_h}$. The fused representation is obtained by a gated weighted summation over the activated granularities: $\bar{\mathbf{E}} = \sum_{i \in \mathcal{I}_{\text{valid}}} \alpha_i \tilde{\mathbf{E}}_i$, $\alpha_i = \tilde{s}_i / \sum_{j \in \mathcal{I}_{\text{valid}}} \tilde{s}_j$.

Sample-level Result. Finally, the representations from all coarse segments are concatenated to form the encoder output

$$\mathbf{H} = \text{Concat}(\bar{\mathbf{E}}_1, \dots, \bar{\mathbf{E}}_N) \in \mathbb{R}^{\tilde{T} \times D_h}, \quad (3)$$

where $\tilde{T} = \sum_{n=1}^N M_n$ and M_n is the embedding sequence length of the n -th segment, forming the representation sequence for the given time series sample \mathbf{X} .

Unlike prior approaches such as Chen et al. (2024); Zhang et al. (2024), which impose a *static* multi-scale partitioning over the entire time series, our method (i) dynamically adapts the tokenization granularity at the *segment level*. (ii) decouples temporal heterogeneity from a fixed representational scale by explicitly and dynamically assigning patch size via routing and multi-granularity encoding, enabling more effective *intra-patch representation learning*. This adaptive behavior cannot be achieved via globally predefined scales applied statically and is empirically validated

in Section 4.4.1. As a result, varying temporal patterns are modeled via the lightweight Mixture-of-Size Encoder, reducing the burden of subsequent model parameterization.

3.3. Heterogeneity-Aware Transformer

Following Mixture-of-Size Encoder, the fused representation $\mathbf{H} \in \mathbb{R}^{\tilde{T} \times D_h}$ is processed by a Heterogeneity-Aware Transformer, a stack of standard Transformer (Vaswani et al., 2017) encoder blocks, yielding representations $\mathbf{H}^{\text{en}} \in \mathbb{R}^{\tilde{T} \times D_h}$ that are subsequently fed to the prediction head. To inject temporal information into the self-attention mechanism, we propose Dynamic Rotary Position Embedding (DRoPE). Unlike static encodings such as Vaswani et al. (2017); Su et al. (2024), DRoPE adaptively calibrates temporal structure to account for instance-specific periodicities and the varying physical durations of dynamic patches.

Base Structure of DRoPE. Our dynamic position encoding is based on the standard Rotary Position Embedding (RoPE) (Su et al., 2024), where a hidden vector $\mathbf{z} \in \mathbb{R}^{D_h}$ (a query or key) at token index $t \in [1, \tilde{T}]$ is treated as a set of $D_h/2$ complex numbers. Each pair is rotated by an angle proportional to the position t and a fixed frequency θ_d as below, where $d \in [0, D_h/2 - 1]$ indexes the dimension:

$$f_{\text{DRoPE}}(\mathbf{z}, t) = (\mathbf{z}_{2d} + i\mathbf{z}_{2d+1})e^{it\theta_d} \quad (4)$$

Here the frequencies are traditionally pre-defined as $\theta_d = b^{-2d/D_h}$. DRoPE generalizes this formulation by dynamically transforming both the frequency θ and the token position t . A detailed derivation of the RoPE calculation is provided in Appendix D.4.

Instance-Level Frequency Modulation. Standard RoPE uses a uniform frequency θ for all sequences, failing to capture the unique periodic structures of heterogeneous time series (analysis in Theorem D.1). We propose to modulate the base frequencies using instance-specific spectral features. Specifically, given a time series input \mathbf{X} , we extract the magnitudes of the first ω low-frequency components via Fast Fourier Transform, denoted as \mathbf{X}_{fft} . A lightweight MLP maps these features to a scaling factor γ and a bias β , to produce *adaptive frequencies* θ_{inst} :

$$\theta_{\text{inst},d} = \gamma_d \cdot \theta_d + \beta_d, \text{ where } \gamma, \beta = \text{MLP}(\mathbf{X}_{\text{fft}}) \quad (5)$$

This affine transformation allows KAIROS to re-scale the temporal rotation based on the dominant information like trends and seasonalities in the specific time series instance.

Granularity-Aware Position Calibration. In our multi-granularity framework, the discrete token index t is no longer an accurate proxy for time because different tokens represent different physical durations, a direct consequence of the granularity routing and tokenization in our

Mixture-of-Size Encoder, as described in Section 3.2. To maintain temporal consistency across mixed patch sizes, we replace the integer index t with a calibrated position $\tilde{t} = \sum_{k=1}^{t-1} \bar{P}_k / \bar{P}_{g,\min}$, where \bar{P}_k is the patch size of the k -th token and $\bar{P}_{g,\min} = \min\{P_i\}_{i=1}^G$ is the globally minimum patch size of the finest granularity.

The resulting DRoPE operation unifies these two components, rotating the hidden vector \mathbf{z} at position t as follows:

$$f_{\text{DRoPE}}(\mathbf{z}, t) = (\mathbf{z}_{2d} + i\mathbf{z}_{2d+1})e^{i\tilde{t}\cdot\theta_{\text{inst},d}} \quad (6)$$

By measuring relative distances in terms of absolute physical time and instance-specific frequencies, DRoPE enables the Transformer to learn consistent temporal dependencies considering the diverse encoding granularity and the intrinsic properties of the data sample.

3.4. Multi-Patch Decoder

To mitigate the error accumulation typical of patch-wise autoregressive decoding while maintaining structural flexibility, KAIROS utilizes a Multi-Patch Decoder. This component forecasts J future patches in parallel, effectively decoupling the prediction horizon from iterative dependencies. We first introduce a sequence of J learnable forecast tokens, $\mathbf{Q}_{\text{forecast}} = \{\mathbf{q}_1, \dots, \mathbf{q}_J\}$. Multi-Patch Decoder processes these token embeddings with the latent representations $\mathbf{H}^{\text{en}} \in \mathbb{R}^{\tilde{T} \times D_h}$ from the above Heterogeneity-Aware Transformer through cross-attention, to produce a sequence of latent forecasting embeddings $\mathbf{h}^{\text{de}} \in \mathbb{R}^{J \times D_h}$.

Each embedding \mathbf{h}_j^{de} is then projected into the observation space via a shared prediction head, which is implemented as a residual FFN block (Das et al., 2024), to generate a future patch of length $H_s = \lceil H/J \rceil$ as

$$\hat{\mathbf{Y}}_{(j-1)H_s+1:jH_s} = \text{ResidualFFN}(\mathbf{h}_j^{\text{de}}), \quad j \in [1, J] \quad (7)$$

This multi-token design is strategically for two objectives regarding predominant forecasting paradigms. (i) *Error mitigation and efficiency*: Compared to conventional single-step autoregressive models (Ansari et al., 2024; Liu et al., 2024c), predicting J patches in parallel improves computational efficiency and mitigates cumulative error by reducing iterative decoding steps. (ii) *Horizon flexibility*: Unlike models that generate a single larger patch (Das et al., 2024), our approach offers superior granularity for variable prediction horizons. By assembling the forecast from the specific subset of tokens required, KAIROS ensures high-fidelity alignment with the target length and avoids the imprecise truncation associated with oversized outputs. We provide a detailed analysis of this design in Appendix B. By combining the Mixture-of-Size Encoder for adaptive input processing with this Multi-Patch Decoder for flexible output generation, KAIROS achieves a unified and parameter-efficient framework for zero-shot time series forecasting.

3.5. Training Corpus

For pre-training, we curated the Predictability-Stratified Time Series (PreSTS) corpus, comprising over 300 billion time points. PreSTS integrates large-scale real-world time series from diverse domains and a complementary synthetic dataset to ensure broad coverage. All test sets from the GIFT-Eval (Aksu et al., 2024) and TSLib (Wang et al., 2024b) benchmarks are explicitly excluded to prevent data leakage. While dataset diversity is widely regarded as essential for TSFM training, recent studies indicate that low-predictability or anomalous sequences can substantially impair forecasting (Cheng et al., 2024). To address this, we stratify real-world datasets into five tiers based on predictability and assign higher sampling probabilities to more predictable data during training. This strategy promotes stable and high-quality pre-training without compromising data diversity. Further details are provided in Appendix E.1.

4. Experiment

In this section, we assess the performance of KAIROS and its components by addressing three research questions. **RQ1**: Does KAIROS achieve superior zero-shot generalization capabilities while maintaining parameter efficiency compared to previous methods? (Section 4.2) **RQ2**: Does the Mixture-of-Size Encoder effectively handle time series heterogeneity by adapting its granularity based on local information density? (Section 4.3 and 4.4.1) **RQ3**: Does DRoPE effectively generate customized position embeddings tailored to the unique temporal structure of each time series instance? (Section 4.3 and 4.4.2)

4.1. Experiment Settings

4.1.1. EVALUATION DATASETS AND METRIC

To comprehensively evaluate our proposed method, we conducted zero-shot assessments on two well-known public benchmarks: GIFT-Eval (Aksu et al., 2024) and Time-Series-Library (TSLib) (Wang et al., 2024b). We train KAIROS in three sizes: mini (10M), small (23M) and base (53M). The training details are provided in Appendix D.1.

Benchmarks. The GIFT-Eval benchmark comprises 97 tasks spanning short- (55), medium- (21), and long-term (21) horizons, facilitating a comprehensive assessment. For TSLib, we selected the ETT and Weather (Zhou et al., 2021) datasets, consistent with Time-MoE (Shi et al., 2024). To test adaptability to diverse frequencies, we also included the Saugeen datasets (Godaheva et al., 2021), denoted as Saugeen (D) and Saugeen (W) for daily and weekly intervals, respectively. The detailed description of the evaluation datasets, splitting configurations, and evaluation length selection are provided in Appendix E.2 and E.3.

Table 1. Performance evaluation on the GIFT-Eval. We evaluate using normalized MASE and CRPS (Section 4.1.1). Baselines encompass statistical, Deep Learning (DL), and TSFM methods, with TSFMs categorized into TestData Leakage and Zero-Shot following official protocols. TestData Leakage signifies that the model’s training set included test data, whereas Zero-Shot indicates that the model was trained without any data from the test set or its corresponding training split. Baseline results are officially reported by GIFT-Eval.

Type	Statistical	DL (Full-Shot)			TSFMs (TestData Leakage)				TSFMs (Zero-Shot)					
Method	Seasonal Naïve	DLinear	PTST	TTM	Chronos	Chronos Bolt	TimesFM	Moirai	VisionTS	Ying.	Toto	Sundial	KAIROS _s (ours)	KAIROS _b (ours)
#Params	-	-	-	5M	709M	205M	500M	311M	112M	300M	151M	128M	23M	53M
MASE ↓	1.000	1.061	0.849	1.020	0.870	0.808	0.758	0.875	0.863	0.798	0.750	0.750	<u>0.748</u>	0.738
CRPS ↓	1.000	0.846	0.587	0.873	0.574	0.574	0.550	0.599	0.755	<u>0.548</u>	0.517	0.559	0.554	<u>0.548</u>

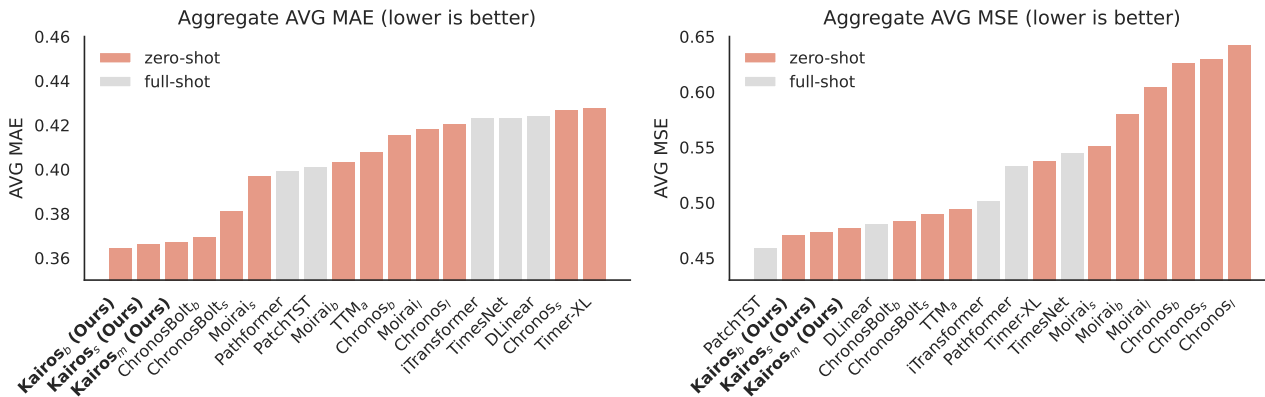


Figure 3. Zero-shot performance on TSLib averaged over prediction lengths {96, 192, 336, 720}. The subscripts *l*, *b*, *s*, *m*, and *a* represent model sizes of large, base, small, mini and advanced, respectively. The complete experimental results are presented in Appendix F.

Metric. In our evaluation of GIFT-Eval, consistent with prior research (Auer et al., 2025; Liu et al., 2025), we employ the official Mean Absolute Scaled Error (MASE) and Continuous Ranked Probability Score (CRPS) metrics to assess point and probabilistic forecasting performance, respectively. These metrics are first normalized by the Seasonal Naïve baseline for each individual task. The final score is then computed as the geometric mean of these normalized values. For the TSLib benchmark, we followed previous works (Liu et al., 2023; 2024c; Nie et al., 2023) by adopting Mean Squared Error (MSE) and Mean Absolute Error (MAE) to evaluate time series forecasting performance. The metric calculations are detailed in Appendix D.2.1.

4.1.2. COMPARED METHODS

We compare KAIROS with several state-of-the-art models, including TSFMs such as Sundial (Liu et al., 2025), Toto (Cohen et al., 2025), YingLong (Wang et al., 2025), VisionTS (Chen et al., 2025), Time-MoE (Shi et al., 2024), ChronosBolt (Ansari et al., 2024), TTM (Ekambaram et al., 2024), Moirai (Woo et al., 2024), Timer-XL (Liu et al., 2024c), TimesFM-2.0 (Das et al., 2024), Chronos (Ansari et al., 2024), and advanced full-shot deep learning models, including PatchTST (Nie et al., 2023), DLinear (Zeng et al., 2022), iTransformer (Liu et al., 2023), Pathformer (Chen et al., 2024), and TimesNet (Wu et al., 2022).

4.2. Zero-shot Evaluation

Finding 1: KAIROS achieves superior zero-shot forecasting performance with significantly higher parameter efficiency. On the GIFT-Eval benchmark, as presented in Table 1, KAIROS_{base} (53M) achieves the best MASE and the second-best CRPS among state-of-the-art task-specific deep learning methods and other TSFMs. Notably, KAIROS_{small} (23M) surpasses both Toto and Sundial in MASE, despite having a parameter count that is 6.6 and 5.6 times smaller, respectively. On the TSLib benchmark, as shown in Figure 3, our lightweight KAIROS_{mini} (10M) surpasses the performance of both recent advanced TSFMs and the majority of full-shot deep learning models. These results confirm that KAIROS delivers a significant improvement in predictive capability without relying on massive scale.

4.3. Ablation Study

Finding 2: The synergistic integration of Mixture-of-Size Encoding, DRoPE, and the Multi-Patch Decoding is critical for adapting to heterogeneous time series and achieving superior forecasting performance. Table 2 details the component-wise contributions. (i) *Encoder Design:* KAIROS outperforms variants using fixed patch sizes or excluding null experts, confirming that dynamic, sparse multi-granularity modeling is critical for capturing diverse tempo-

ral patterns. (ii) *Positional Embedding*: DRoPE proves superior to standard RoPE (Su et al., 2024). Our ablation further isolates the gains from *Instance-Level Frequency Modulation* and *Granularity-Aware Position Calibration*, verifying the benefit of adapting to both spectral heterogeneity and physical time distortion caused by dynamic patching. (iii) *Decoding Strategy*: The Multi-Patch Decoding shows clear superiority over standard single-patch autoregressive decoding. The integration of both components yielded the best performance across 97 GIFT-Eval tasks, which validates the superiority of our designs. Furthermore, the performance gap widens as the forecast horizon increases, demonstrating KAIROS’s superior long-term forecasting capability.

Table 2. Ablation study comparing encoder design, positional embedding and decoder strategy. Models were evaluated using the normalized MASE (detailed in Section 4.1.1) across individual prediction horizons and as an aggregate across all tasks.

Model Variants	Short	Medium	Long	AVG
Impact of Encoder Design				
w/ Fixed Patch Size ($P = 32$)	0.724	0.802	0.820	0.761
w/ Mixture-of-Size (w/o Null Experts)	0.720	0.770	0.800	0.748
Impact of Positional Embedding				
w/ Standard RoPE (Fixed θ)	0.729	0.807	0.835	0.767
w/ Only Instance-Level Frequency Modulation	0.719	0.767	0.797	0.746
w/ Only Granularity-Aware Position Calibration	0.727	0.796	0.807	0.758
Impact of Decoder Strategy				
w/ Single-Patch Autoregressive	0.705	0.794	0.848	0.753
KAIROS (Full Model)	0.709	0.761	0.794	0.738

4.4. Model Analysis

4.4.1. MIXTURE-OF-SIZE TOKENIZATION ANALYSIS

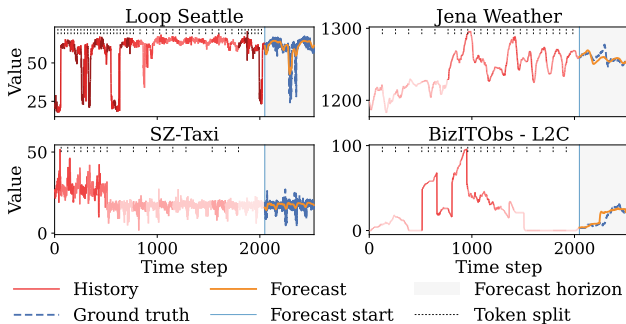


Figure 4. Adaptive tokenization visualization. Tokens are demarcated by dotted lines and varying colors, where deeper red curves indicate finer granularity. KAIROS adapts granularity to information density, applying finer processing to volatile regions.

Finding 3: KAIROS demonstrates adaptive capability to varying information densities, enabling it to model complex temporal dynamics with appropriate granularity. Instead of enforcing a uniform resolution, KAIROS dynamically routes segments to optimal granularity based on local information. As visualized in Figure 4, KAIROS strategically allocates fine-grained tokens to regions with abrupt changes or high volatility, while employing coarse-grained tokens for sta-

ble trends. This adaptive allocation mechanism reduces computational redundancy on low-information segments, allowing the model to achieve superior performance with a compact parameter budget compared to rigid architectures. See Appendix C for a detailed inference speed analysis.

4.4.2. DROPE ANALYSIS

Table 3. Causal analysis of adaptive modulation by DRoPE. We evaluate the impact of disrupting or removing the instance-wise θ adjustment. Degradation indicates relative performance drop compared to DRoPE.

Method	DRoPE (Ours)	Intra-Dataset Shuffle	Standard RoPE (Fixed θ)	Inter-Dataset Shuffle
MASE ↓	0.738	0.751	0.767	0.947
Degradation	–	-1.76%	-3.93%	-28.32%

Finding 4: Modulating RoPE frequencies θ instance-wise can indeed better model time series temporal relationships. To verify that DRoPE’s performance gains stem from its instance-specific θ_{inst} modulation, we designed control experiments that disrupt this mechanism (Table 3; Appendix E.4): (i) Intra-Dataset Shuffle: randomly permute θ_{inst} across instances within the same dataset; (ii) Inter-Dataset Shuffle: assign θ_{inst} from instances of different datasets; (iii) Fixed RoPE: use standard RoPE without any modulation. The results reveal a clear performance gradient (DRoPE \succ Intra-Shuffle \succ Fixed RoPE \succ Inter-Shuffle), indicating that DRoPE learns instance-specific representations to modulate θ . Intra-Dataset Shuffle outperforms Fixed RoPE, as samples within the same dataset share similar spectral characteristics, allowing shuffled θ_{inst} to remain partially compatible. However, Intra-Dataset Shuffle still incurs a 1.76% degradation compared to DRoPE, suggesting that instance-level adaptation contributes to the performance gains beyond dataset-level statistics. Inter-Dataset Shuffle yields the worst results (28.32% degradation), as θ_{inst} from different datasets cannot capture the target series’ temporal dynamics. These results collectively validate the effectiveness of instance-level θ_{inst} adaptation in DRoPE.

5. Conclusions

We introduce KAIROS, a parameter-efficient foundation model explicitly tailored for time series heterogeneity. Its architecture features three key innovations: a Mixture-of-Size Encoder for adaptive granularity, a Heterogeneity-Aware Transformer with Dynamic RoPE for instance-specific temporal calibration, and a Multi-Patch Decoder for efficient parallel forecasting. Extensive experiments demonstrate that KAIROS achieves superior performance, validating the necessity of aligning architectural inductive biases with the structural nuances of time series data. One limitation of our current approach is that KAIROS relies on channel-independent modeling (Nie et al., 2023) to support multivari-

ate time series and does not explicitly capture inter-variable dependencies. Future work aims to model these interactions and extend KAIROS to tasks beyond forecasting.

Impact Statement

Our work on KAIROS is foundational research focused on advancing parameter-efficient and adaptive time series modeling. We anticipate several positive societal impacts: (i) promoting sustainable AI by significantly reducing the computational resources and energy required for large-scale deployment; (ii) enhancing decision-making in dynamic environments (e.g., energy, retail) through improved modeling of heterogeneous temporal patterns; and (iii) providing a high-quality data curation methodology via the PreSTS corpus to improve model performance.

While we do not foresee immediate negative societal consequences, we recognize that advanced predictive technologies carry inherent risks of misuse. Consequently, rigorous ethical oversight is therefore essential to guarantee that such predictive capabilities serve the public interest.

References

- Achiam, J., Adler, S., Agarwal, S., Ahmad, L., Akkaya, I., Aleman, F. L., Almeida, D., Altenschmidt, J., Altman, S., Anadkat, S., et al. Gpt-4 technical report. *arXiv preprint arXiv:2303.08774*, 2023.
- Agarwal, N., Ali, A., Bala, M., Balaji, Y., Barker, E., Cai, T., Chattopadhyay, P., Chen, Y., Cui, Y., Ding, Y., et al. Cosmos world foundation model platform for physical ai. *arXiv preprint arXiv:2501.03575*, 2025.
- Aksu, T., Woo, G., Liu, J., Liu, X., Liu, C., Savarese, S., Xiong, C., and Sahoo, D. Gift-eval: A benchmark for general time series forecasting model evaluation. In *NeurIPS Workshop on Time Series in the Age of Large Models*, 2024.
- Ansari, A. F., Stella, L., Turkmen, C., Zhang, X., Mercado, P., Shen, H., Shchur, O., Rangapuram, S. S., Pineda Arango, S., Kapoor, S., Zschiegner, J., Maddix, D. C., Mahoney, M. W., Torkkola, K., Gordon Wilson, A., Bohlke-Schneider, M., and Wang, Y. Chronos: Learning the language of time series. *Transactions on Machine Learning Research*, 2024. ISSN 2835-8856. URL <https://openreview.net/forum?id=gerNCVqqtR>.
- Auer, A., Podest, P., Klotz, D., Böck, S., Klambauer, G., and Hochreiter, S. Tirez: Zero-shot forecasting across long and short horizons with enhanced in-context learning. *arXiv preprint arXiv:2505.23719*, 2025.
- Box, G. E., Jenkins, G. M., Reinsel, G. C., and Ljung, G. M. *Time series analysis: forecasting and control*. John Wiley & Sons, 2015.
- Chen, M., Shen, L., Li, Z., Wang, X. J., Sun, J., and Liu, C. Visionts: Visual masked autoencoders are free-lunch zero-shot time series forecasters. In *Forty-second International Conference on Machine Learning*, 2025.
- Chen, P., Zhang, Y., Cheng, Y., Shu, Y., Wang, Y., Wen, Q., Yang, B., and Guo, C. Pathformer: Multi-scale transformers with adaptive pathways for time series forecasting. *arXiv preprint arXiv:2402.05956*, 2024.
- Cheng, H., Wen, Q., Liu, Y., and Sun, L. Robusttsf: Towards the theory and design of robust time series forecasting with anomalies. In *The Twelfth International Conference on Learning Representations*, 2024.
- Cohen, B., Khwaja, E., Doubli, Y., Lemaachi, S., Lettieri, C., Masson, C., Miccinilli, H., Ramé, E., Ren, Q., Ros-tamizadeh, A., et al. This time is different: An observability perspective on time series foundation models. *arXiv preprint arXiv:2505.14766*, 2025.
- Das, A., Kong, W., Sen, R., and Zhou, Y. A decoder-only foundation model for time-series forecasting. In *Forty-first International Conference on Machine Learning*, 2024.
- Ekambaram, V., Jati, A., Dayama, P., Mukherjee, S., Nguyen, N. H., Gifford, W. M., Reddy, C., and Kalagnanam, J. Tiny time mixers (ttms): Fast pre-trained models for enhanced zero/few-shot forecasting of multi-variate time series, 2024.
- Gage, P. A new algorithm for data compression. *The C Users Journal*, 12(2):23–38, 1994.
- Godahewa, R., Bergmeir, C., Webb, G. I., Hyndman, R. J., and Montero-Manso, P. Monash time series forecasting archive. In *Neural Information Processing Systems Track on Datasets and Benchmarks*, 2021.
- Graf, L., Ortner, T., Woł̄sniak, S., Pantazi, A., et al. Flowstate: Sampling rate invariant time series forecasting. *arXiv preprint arXiv:2508.05287*, 2025.
- Gruver, N., Finzi, M., Qiu, S., and Wilson, A. G. Large language models are zero-shot time series forecasters. *Advances in Neural Information Processing Systems*, 36: 19622–19635, 2023.
- Jacobs, R. A., Jordan, M. I., Nowlan, S. J., and Hinton, G. E. Adaptive mixtures of local experts. *Neural computation*, 3(1):79–87, 1991.

- Jin, P., Zhu, B., Yuan, L., and YAN, S. Moe++: Accelerating mixture-of-experts methods with zero-computation experts. In *The Thirteenth International Conference on Learning Representations*, 2024.
- Kirillov, A., Mintun, E., Ravi, N., Mao, H., Rolland, C., Gustafson, L., Xiao, T., Whitehead, S., Berg, A. C., Lo, W.-Y., Dollár, P., and Girshick, R. Segment anything. *arXiv:2304.02643*, 2023.
- Lim, B., Arık, S. Ö., Loeff, N., and Pfister, T. Temporal fusion transformers for interpretable multi-horizon time series forecasting. *International journal of forecasting*, 37(4):1748–1764, 2021.
- Lin, H., Lv, A., Song, Y., Zhu, H., Yan, R., et al. Mixture of in-context experts enhance llms’ long context awareness. *Advances in Neural Information Processing Systems*, 37: 79573–79596, 2024.
- Liu, A., Feng, B., Xue, B., Wang, B., Wu, B., Lu, C., Zhao, C., Deng, C., Zhang, C., Ruan, C., et al. Deepseek-v3 technical report. *arXiv preprint arXiv:2412.19437*, 2024a.
- Liu, X., Liu, J., Woo, G., Aksu, T., Liang, Y., Zimmermann, R., Liu, C., Savarese, S., Xiong, C., and Sahoo, D. Moirai-moe: Empowering time series foundation models with sparse mixture of experts. *arXiv preprint arXiv:2410.10469*, 2024b.
- Liu, Y., Hu, T., Zhang, H., Wu, H., Wang, S., Ma, L., and Long, M. itransformer: Inverted transformers are effective for time series forecasting. *arXiv preprint arXiv:2310.06625*, 2023.
- Liu, Y., Qin, G., Huang, X., Wang, J., and Long, M. Timerxl: Long-context transformers for unified time series forecasting. *arXiv preprint arXiv:2410.04803*, 2024c.
- Liu, Y., Qin, G., Shi, Z., Chen, Z., Yang, C., Huang, X., Wang, J., and Long, M. Sundial: A family of highly capable time series foundation models. *arXiv preprint arXiv:2502.00816*, 2025.
- Nie, Y., Nguyen, N. H., Sinthong, P., and Kalagnanam, J. A time series is worth 64 words: Long-term forecasting with transformers. In *International Conference on Learning Representations*, 2023.
- Oreshkin, B. N., Carпов, D., Chapados, N., and Bengio, Y. N-BEATS: Neural basis expansion analysis for interpretable time series forecasting. In *International Conference on Learning Representations*, 2020. URL <https://openreview.net/forum?id=rlecqn4YwB>.
- Rasul, K., Ashok, A., Williams, A. R., Khorasani, A., Adamopoulos, G., Bhagwatkar, R., Biloš, M., Ghonia, H., Hassen, N., Schneider, A., et al. Lag-llama: Towards foundation models for time series forecasting. In *R0-FoMo: Robustness of Few-shot and Zero-shot Learning in Large Foundation Models*, 2023.
- Sennrich, R., Haddow, B., and Birch, A. Neural machine translation of rare words with subword units. In Erk, K. and Smith, N. A. (eds.), *Proceedings of the 54th Annual Meeting of the Association for Computational Linguistics (Volume 1: Long Papers)*, pp. 1715–1725, Berlin, Germany, August 2016. Association for Computational Linguistics. doi: 10.18653/v1/P16-1162. URL <https://aclanthology.org/P16-1162/>.
- Shazeer, N., Mirhoseini, A., Maziarz, K., Davis, A., Le, Q., Hinton, G., and Dean, J. Outrageously large neural networks: The sparsely-gated mixture-of-experts layer. In *International Conference on Learning Representations*, 2017.
- Shi, X., Wang, S., Nie, Y., Li, D., Ye, Z., Wen, Q., and Jin, M. Time-moe: Billion-scale time series foundation models with mixture of experts, 2024. URL <https://arxiv.org/abs/2409.16040>.
- Su, J., Ahmed, M., Lu, Y., Pan, S., Bo, W., and Liu, Y. Roformer: Enhanced transformer with rotary position embedding. *Neurocomputing*, 568:127063, 2024.
- Vaswani, A., Shazeer, N., Parmar, N., Uszkoreit, J., Jones, L., Gomez, A. N., Kaiser, Ł., and Polosukhin, I. Attention is all you need. *Advances in neural information processing systems*, 30, 2017.
- Wang, S., Wu, H., Shi, X., Hu, T., Luo, H., Ma, L., Zhang, J. Y., and Zhou, J. Timemixer: Decomposable multi-scale mixing for time series forecasting. *arXiv preprint arXiv:2405.14616*, 2024a.
- Wang, X., Zhou, T., Gao, J., Ding, B., and Zhou, J. Output scaling: Yinglong-delayed chain of thought in a large pretrained time series forecasting model. *arXiv preprint arXiv:2506.11029*, 2025.
- Wang, Y., Wu, H., Dong, J., Liu, Y., Wang, C., Long, M., and Wang, J. Deep time series models: A comprehensive survey and benchmark. *arXiv preprint arXiv:2407.13278*, 2024b.
- Woo, G., Liu, C., Kumar, A., Xiong, C., Savarese, S., and Sahoo, D. Unified training of universal time series forecasting transformers. In *Forty-first International Conference on Machine Learning*, 2024.
- Wu, H., Hu, T., Liu, Y., Zhou, H., Wang, J., and Long, M. Timesnet: Temporal 2d-variation modeling for general time series analysis. *arXiv preprint arXiv:2210.02186*, 2022.

Zeng, A., Chen, M., Zhang, L., and Xu, Q. Are transformers effective for time series forecasting? *arXiv preprint arXiv:2205.13504*, 2022.

Zeng, Z., Miao, Y., Gao, H., Zhang, H., and Deng, Z. Adamoe: Token-adaptive routing with null experts for mixture-of-experts language models. In *Findings of the Association for Computational Linguistics: EMNLP 2024*, pp. 6223–6235, 2024.

Zhang, J., Zheng, S., Wen, X., Zhou, X., Bian, J., and Li, J. Elastst: Towards robust varied-horizon forecasting with elastic time-series transformer. *arXiv preprint arXiv:2411.01842*, 2024.

Zheng, C., Gao, Y., Shi, H., Huang, M., Li, J., Xiong, J., Ren, X., Ng, M., Jiang, X., Li, Z., et al. Dape: Data-adaptive positional encoding for length extrapolation. *Advances in Neural Information Processing Systems*, 37:26659–26700, 2024.

Zhou, H., Zhang, S., Peng, J., Zhang, S., Li, J., Xiong, H., and Zhang, W. Informer: Beyond efficient transformer for long sequence time-series forecasting. In *Proceedings of the AAAI conference on artificial intelligence*, volume 35, pp. 11106–11115, 2021.

A. Etymology of KAIROS

KAIROS was chosen for its mythological significance as the Greek god of the “right or critical moment”, reflecting our model’s ability to select the ideal set of granularities and positional encoding for time series characterized by varying information densities and frequencies. Furthermore, this continues a thematic tradition seen in other foundational models we benchmark against, such as Chronos (Ansari et al., 2024) (the personification of time) and Moirai (Woo et al., 2024) (the personifications of destiny).

B. Analysis of Multi-Patch Prediction

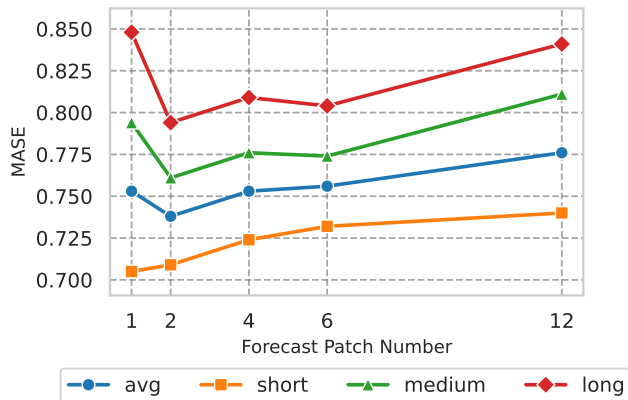


Figure 5. Performance analysis of multi-patch prediction on the GIFT-Eval benchmark across short, medium, and long horizons. We vary the number of forecast patches and find that a forecast patch number of 2 achieves the optimal trade-off, resulting in the best overall performance (lowest normalized MASE).

Unlike task-specific, non-autoregressive models such as TFT (Lim et al., 2021) and Informer (Zhou et al., 2021), which predict all future time points simultaneously, their architecture confines them to forecasting a fixed length identical to the training sequence, precluding variable-length predictions. Conversely, TSFMs typically employ an iterative process: they predict a segment of the sequence, append it to the historical data, and then forecast the subsequent segment, thereby enabling autoregressive predictions of arbitrary length. To mitigate the cumulative errors inherent in this autoregressive methodology, KAIROS introduces forecast tokens designed to predict multiple patches within each autoregressive step.

In this section, we present an analysis of the multi-patch prediction strategy introduced in Section 3.4. During the training phase, we experimented with a range of forecast patch numbers, specifically $J = \{1, 2, 4, 6, 12\}$. The corresponding evaluation results on the GIFT-Eval benchmark are illustrated in Figure 5. Our observations reveal that when $J = 1$, which corresponds to the conventional approach of predicting a single patch (Ansari et al., 2024; Liu et al., 2024c; Das et al., 2024), the model achieves optimal performance in short-term forecasting. However, this method necessitates multiple iterations of autoregressive prediction, leading to a significant degradation in performance for medium- and long-term forecasting.

Conversely, as we increase the forecast patch number J , the number of required autoregressive steps is markedly reduced. For instance, when $J = 2$, the autoregression frequency for medium- and long-term predictions is halved compared to the $J = 1$ case. This reduction yields a substantial improvement in forecasting accuracy over these longer horizons, demonstrating that our proposed multi-patch prediction strategy effectively mitigates the cumulative error inherent in autoregressive processes for medium- and long-term forecasting.

Nevertheless, we noted that the forecasting performance does not improve indefinitely with an increasing the forecast patch number J . We attribute this phenomenon to the escalated difficulty of the prediction task, which hinders the model’s ability to optimize effectively. Ultimately, by evaluating the mean normalized MASE, we identified the optimal trade-off, selecting a forecast patch number of $J = 2$ for KAIROS.

C. Analysis of Inference Speed

To provide a comprehensive view of our model’s efficiency, we benchmarked the single-batch inference speed of KAIROS against several state-of-the-art models. The experimental setup involved an input sequence length of 2048 and a prediction horizon of 96 on a single NVIDIA TITAN RTX GPU. For TTM-Advanced, its maximum supported input length of 1536 was used.

As shown in Table 4, the inference time of KAIROS is on the same order of magnitude as other highly efficient models like ChronosBolt and Moirai. This demonstrates that KAIROS maintains competitive computational efficiency while delivering the superior forecasting accuracy detailed in the main paper. Notably, it is significantly faster than models like Time-MoE, TimesFM, and especially Chronos.

Table 4. Comparison of single-batch inference speeds. All models were tested with an input length of 2048 and an output length of 96, with the exception of TTM-Advanced (*), which used its maximum input length of 1536. Times are averaged per batch and reported in seconds.

Model	Inference Time (s)
TTM-Advanced*	0.009
Timer-XL	0.014
ChronosBolt-Base	0.055
KAIROS-Base (Ours)	0.061
Moirai-Large	0.070
Sundial-Base	0.099
Time-MoE-Large	0.148
TimesFM-2.0	0.202
Chronos-Large	4.901
Toto-Base	13.717

D. Implementation Details

D.1. Training Details

D.1.1. MODEL CONFIGURATIONS

We train KAIROS in three sizes: mini (10M), small (23M) and base (53M) with the detailed model configurations are in Table 5. The base model are trained for 300,000 steps with batch sizes of 512. We employ the AdamW optimizer, a linear decay learning rate adjustment strategy for model optimization. The learning rate for parameters related to DRoPE is set to 1e-5, while the learning rate for others is set to 1e-3. Training is conducted on 4 × NVIDIA A100 GPUs using TF32 precision, which takes only 15 hours for base size.

Table 5. Details of KAIROS model configurations.

	Layers	Heads	d_{model}	d_{ff}	d_{expert}	P	K	G	Z	τ	η_b	w	θ	Params
KAIROS _{mini}	4	4	256	1024	1408	{32, 64, 128}	3	3	2	{0.55, 0.1, 0.05, 0.15, 0.15}	0.01	128	$10000^{-2j/64}$	10M
KAIROS _{small}	4	8	384	1536	1408	{32, 64, 128}	3	3	2	{0.55, 0.1, 0.05, 0.15, 0.15}	0.01	128	$10000^{-2j/64}$	23M
KAIROS _{base}	6	8	512	2048	1408	{32, 64, 128, 256}	4	4	2	{0.55, 0.1, 0.05, 0.15, 0.15}	0.01	128	$10000^{-2j/64}$	53M

D.1.2. LOSS FUNCTION

To better accommodate varied forecast horizons, and following the methodology of ElasTST (Zhang et al., 2024), we build upon the standard quantile loss by assigning distinct weights to each timestep, such that earlier predictions are given greater importance. The model’s parameters are optimized by minimizing the quantile loss with weight decay, formulated as:

$$\mathcal{L} = \frac{1}{B} \sum_{i=1}^B \sum_{t=1}^H \frac{1}{K} \sum_{k=1}^K \omega(t) L_{\alpha_k}(y_{i,t}, q_{i,t}(\alpha_k)), \tag{8}$$

$$\omega(t) = \frac{1}{H}(\ln(H) - \ln(t)), \quad L_\alpha(y, q) = (\alpha - \mathbf{1}_{\{y < q\}})(y - q), \quad (9)$$

where B, H, K are the batch size, forecast horizon, and number of quantiles, respectively; $y_{i,t}$ is the ground truth value, $q_{i,t}(\alpha_k)$ is the k -th quantile forecast, $\omega(t)$ is the weight at each time step t , and L_{α_k} denotes the pinball loss function. Empirically, we set $K = 9$ and use quantile levels of $\alpha = 0.1, 0.2, \dots, 0.9$.

D.2. Evaluation Details

D.2.1. METRIC

GIFT-Eval. GIFT-Eval employs the Mean Absolute Scaled Error (MASE) and the Continuous Ranked Probability Score (CRPS) to assess the performance of point and probabilistic forecasts, respectively. Following the official evaluation protocol, we normalize the metrics for each task using a seasonal naïve baseline and subsequently aggregate the scores across all tasks via the geometric mean.

TSLib. We adopt mean square error (MSE) and mean absolute error (MAE) as evaluation metrics. These metrics are calculated as follows:

$$\text{MSE} = \frac{1}{H} \sum_{i=1}^H (x_i - \hat{x})^2, \quad \text{MAE} = \frac{1}{H} \sum_{i=1}^H |x_i - \hat{x}| \quad (10)$$

where x_i is the ground truth and \hat{x}_i is the prediction for the i -th future time point.

D.2.2. STRIDE

Due to the significant inference latency of our baseline, Chronos (Ansari et al., 2024), we set the evaluation stride to 96 to enhance evaluation efficiency without compromising fairness. This setting is consistent with the protocols of Moirai (Woo et al., 2024), Moirai-MoE (Liu et al., 2024b), and the GIFT-Eval benchmark (Aksu et al., 2024), all of which set the stride equal to the prediction length. Additionally, the original Chronos paper evaluates the model on only a single window per dataset. Therefore, we wish to emphasize a critical point: while the specific numerical results would likely vary with a different stride, our chosen protocol is applied uniformly to all models under evaluation, ensuring a fair and equitable comparison.

D.3. Mixture-of-Size Encoder

D.3.1. AUXILIARY-LOSS-FREE LOAD BALANCING

In this section, we elaborate on the details of bias previously introduced in Section 3.2. In order to ensure that different experts are adequately trained and to control the distribution ratios of various patch sizes, we employ an Auxiliary-Loss-Free Load Balancing method similar to that used in DeepSeek-V3 (Liu et al., 2024a). Specifically, we sum the normalized gating value of the i -th expert activated throughout the entire sequence to obtain L_i :

$$L_i = \sum_{n=1}^N \alpha_{n,i}, \quad (11)$$

where

$$\alpha_{n,i} = \frac{g_{n,i}}{\sum_{j=1}^S g_{n,j}}. \quad (12)$$

We define a target load distribution $\tau = (\tau_1, \tau_2, \dots, \tau_S)$, where τ_i is the desired proportion of the total load for expert i , satisfying $\sum_{j=1}^S \tau_j = 1$. Next, we update the bias term \mathbf{b}_i using L_i and τ :

$$\mathbf{b}_i \leftarrow \mathbf{b}_i + \eta_b \cdot \frac{\tau_i \cdot \sum_{j=1}^S L_j - L_i}{\sum_{j=1}^S L_j}, \quad (13)$$

where η_b is a hyper-parameter to govern the magnitude of this adjustment and is referred to as the bias update speed.

In practical implementation, \mathbf{b}_i is updated once per batch, i.e., L_i denotes the sum of the normalized gating values for the i -th expert across all sequences within the entire batch. At the end of each step, the bias term \mathbf{b}_i for each expert is adjusted. This dynamic adjustment of \mathbf{b}_i aims to balance the workload across the experts according to the desired distribution by influencing future top-K selections, while also steering the patches-to-expert affinity scores $s'_{n,i}$ in subsequent batches, ensuring that the actual load distribution L_i progressively aligns with the target distribution τ_i , thereby promoting balanced expert utilization over time.

D.3.2. DEFINITION OF THE EXPANSION FUNCTION

In this section, we provide the formal definition for the function $\text{Expand}(\cdot)$ within the Mixture-of-Size Fusion stage, as introduced in Section 3.2.

Consider a single time series segment \mathbf{x} of length P . During the Top- K Granularity Routing, a set of valid experts $\mathcal{I}_{\text{valid}}$ is activated. Let P_{\min} denote the finest granularity among these activated experts:

$$P_{\min} = \min\{P_j \mid j \in \mathcal{I}_{\text{valid}}\}. \quad (14)$$

Consequently, the target sequence length for alignment is defined as $M = \lceil P/P_{\min} \rceil$.

For an activated granularity level i with patch size P_i , the encoding process yields a sequence of embeddings $\mathbf{E}_i = [e_{i,1}, \dots, e_{i,M_i}]$, where $M_i = \lceil P/P_i \rceil$. Due to the nested design of patch sizes, the ratio $R_i = P_i/P_{\min}$ is strictly a positive integer.

The function $\text{Expand}(\mathbf{E}_i)$ maps the coarser embedding sequence to the finest temporal resolution by repeating each embedding vector R_i times. Formally, the k -th element of the expanded sequence $\tilde{\mathbf{E}}_i \in \mathbb{R}^{M \times D_h}$ is derived from the original sequence via index mapping:

$$\tilde{e}_{i,m} = e_{i,\lceil m/R_i \rceil}, \quad \text{for } m = 1, \dots, M. \quad (15)$$

In vector notation, this operation can be expressed as:

$$\text{Expand}(\mathbf{E}_i) = \underbrace{[e_{i,1}, \dots, e_{i,1}]}_{R_i \text{ times}}, \dots, \underbrace{[e_{i,M_i}, \dots, e_{i,M_i}]}_{R_i \text{ times}}. \quad (16)$$

We now illustrate the computational process with the following example. Let the setup be as follows:

- Segment length: $P = 128$.
- Set of available granularity patch sizes: $\{P_1, P_2, P_3\} = \{32, 64, 128\}$.
- Number of null experts: $Z = 2$.
- Top- K selection: $K = 2$.

Suppose for a specific segment \mathbf{x} , the router activates experts corresponding to granularity levels 1 and 3 (i.e., $\mathcal{I}_{\text{valid}} = \{1, 3\}$). The finest activated resolution is $P_{\min} = \min(32, 128) = 32$. The target aligned sequence length is $M = 128/32 = 4$.

The expansion process for each expert is computed as follows:

- **For Expert 1 ($P_1 = 32$):**

The number of original patches is $M_1 = 128/32 = 4$. The embedding sequence is $\mathbf{E}_1 = [e_{1,1}, e_{1,2}, e_{1,3}, e_{1,4}]$. The repetition factor is $R_1 = 32/32 = 1$.

$$\tilde{\mathbf{E}}_1 = \text{Expand}(\mathbf{E}_1) = [e_{1,1}, e_{1,2}, e_{1,3}, e_{1,4}]. \quad (17)$$

Since this expert operates at the finest activated resolution, the expansion is an identity mapping.

- **For Expert 3 ($P_3 = 128$):**

The number of original patches is $M_3 = 128/128 = 1$. The embedding sequence consists of a single vector $\mathbf{E}_3 = [e_{3,1}]$. The repetition factor is $R_3 = 128/32 = 4$.

$$\tilde{\mathbf{E}}_3 = \text{Expand}(\mathbf{E}_3) = [e_{3,1}, e_{3,1}, e_{3,1}, e_{3,1}]. \quad (18)$$

The single coarse embedding is broadcast across all 4 time steps to align with the target resolution.

- **Hypothetical Case for Expert 2** ($P_2 = 64$):

Although Expert 2 was not activated in this example, if it were processed, $M_2 = 128/64 = 2$ and $R_2 = 64/32 = 2$. The expansion would be:

$$\tilde{\mathbf{E}}_2 = [e_{2,1}, e_{2,1}, e_{2,2}, e_{2,2}]. \quad (19)$$

By explicitly aligning all representations to the finest resolution P_{\min} via $\text{Expand}(\cdot)$, KAIROS ensures that the subsequent weighted summation $\bar{\mathbf{E}} = \sum_{i \in \mathcal{I}_{\text{valid}}} \alpha_i \tilde{\mathbf{E}}_i$ is performed on element-wise compatible tensors, effectively fusing global context with local details.

D.4. Dynamic Rotary Position Embedding (DRoPE)

In this section, we provide a more detailed description of the DRoPE implementation discussed in Section 3.3. We first introduce the principles of Rotary Position Embedding (RoPE) (Su et al., 2024) in detail, and then provide corresponding supplementary information on the DRoPE implementation.

D.4.1. DETAILS OF ROPE

The core idea of RoPE is to rotate segments of the query and key vectors by an angle proportional according to their absolute position in the sequence. This allows the model to discern relative positions through the geometry of these rotations, without needing explicit calculation of relative distances. Throughout this subsection, we use m and n to denote generic token positions.

Specifically, RoPE operates on vectors of an even dimension, denoted as D_h . For a vector e (representing a query \mathbf{q} or a key \mathbf{k} in self-attention) at position m , it is transformed by a rotation matrix \mathbf{R}_m . This matrix is block-diagonal, composed of $D_h/2$ individual 2×2 rotation blocks. Each block $\mathbf{R}_{m,d}$ acts on a pair of dimensions (e_{2d}, e_{2d+1}) of the vector:

As introduced in Section 3.3, RoPE applies a rotation to input vector. This rotation is applied to pairs of dimensions (e_{2d}, e_{2d+1}) , and can be concisely expressed using complex form:

$$f_{\text{RoPE}}(\mathbf{z}, m) = (z_{2d} + iz_{2d+1})e^{im\theta_d}, \quad (20)$$

where θ_d is the angular frequency. Here, i denotes the imaginary unit. This multiplication by $e^{im\theta_d}$ corresponds to a rotation in the complex plane. For the real-valued components z_{2d} and z_{2d+1} , this operation is equivalent to applying the following 2×2 rotation matrix $\mathbf{R}_{m,d}$:

$$\mathbf{R}_{m,d} = \begin{bmatrix} \cos(m\theta_d) & -\sin(m\theta_d) \\ \sin(m\theta_d) & \cos(m\theta_d) \end{bmatrix}, \quad (21)$$

Here, m is the absolute position of the token. The term θ_d represents a predefined angular frequency for the d -th pair of dimensions ($d \in [0, D_h/2 - 1]$), typically defined as $\theta_d = b^{-2d/D_h}$.

The full rotation matrix \mathbf{R}_m for position m is thus:

$$\begin{aligned} \mathbf{R}_m &= \text{diag}(\mathbf{R}_{m,0}, \mathbf{R}_{m,1}, \dots, \mathbf{R}_{m,D_h/2-1}) \\ &= \begin{pmatrix} \cos m\theta_0 & -\sin m\theta_0 & 0 & 0 & \cdots & 0 & 0 \\ \sin m\theta_0 & \cos m\theta_0 & 0 & 0 & \cdots & 0 & 0 \\ 0 & 0 & \cos m\theta_1 & -\sin m\theta_1 & \cdots & 0 & 0 \\ 0 & 0 & \sin m\theta_1 & \cos m\theta_1 & \cdots & 0 & 0 \\ \vdots & \vdots & \vdots & \vdots & \ddots & \vdots & \vdots \\ 0 & 0 & 0 & 0 & \cdots & \cos m\theta_{D_h/2-1} & -\sin m\theta_{D_h/2-1} \\ 0 & 0 & 0 & 0 & \cdots & \sin m\theta_{D_h/2-1} & \cos m\theta_{D_h/2-1} \end{pmatrix}. \end{aligned} \quad (22)$$

$$(23)$$

Let \mathbf{q}_m and \mathbf{k}_n be the original query and key vectors for tokens at positions m and n respectively. After applying RoPE, their new representations become $\mathbf{q}'_m = \mathbf{R}_m \mathbf{q}_m$ and $\mathbf{k}'_n = \mathbf{R}_n \mathbf{k}_n$. The dot product for attention is then:

$$(\mathbf{q}'_m)^\top (\mathbf{k}'_n) = (\mathbf{R}_m \mathbf{q}_m)^\top (\mathbf{R}_n \mathbf{k}_n) = \mathbf{q}_m^\top \mathbf{R}_m^\top \mathbf{R}_n \mathbf{k}_n, \quad (24)$$

due to the properties of rotation matrices, $\mathbf{R}_m^\top \mathbf{R}_n = \mathbf{R}_{n-m}$ we can get:

$$(\mathbf{q}'_m)^\top (\mathbf{k}'_n) = \mathbf{q}_m^\top \mathbf{R}_{n-m} \mathbf{k}_n. \quad (25)$$

This equation shows that the dot product between a query and key vector after rotation inherently depends on their original values $(\mathbf{q}_m, \mathbf{k}_n)$ and their relative positions $(n - m)$. This allows RoPE to integrate relative positional information into the self-attention without any additional learnable parameters or explicit relative position computations.

Equation 25 confirms that the interaction relies on the relative position $n - m$ through the full rotation matrix \mathbf{R}_{n-m} . Since this matrix is block-diagonal, the total interaction is actually composed of independent rotations on disjoint 2D subspaces. The following theorem demonstrates the periodicity of the attention score within each subspace.

Theorem D.1 (Periodic dependence of RoPE attention). *Consider the d -th 2D subspace of the hidden state under RoPE, with angular frequency θ_d , and let $\text{atten}_d(m, n)$ denote this subspace’s contribution to the dot-product attention between positions m and n . Then there exist an amplitude $A_d(m, n) \geq 0$ and a phase $\varphi_d(m, n)$, depending only on the content vectors at m and n , such that*

$$\begin{aligned} \text{atten}_d(m, n) &= A_d(m, n) \cos(\theta_d(m - n) + \varphi_d(m, n)) \\ &\propto \cos(\theta_d(m - n) + \varphi_d(m, n)). \end{aligned} \quad (26)$$

In particular, for fixed content, $\text{atten}_d(m, n)$ is a periodic function of the relative distance $(m - n)$ with period $2\pi/\theta_d$.

Proof. Let $q_{m,d}, k_{n,d} \in \mathbb{C}$ be the complex-valued representations of the d -th 2D subspace for the query and key at positions m and n , respectively, as defined above. Applying RoPE multiplies these components by phase factors $e^{im\theta_d}$ and $e^{in\theta_d}$, yielding

$$q'_{m,d} = q_{m,d} e^{im\theta_d}, \quad k'_{n,d} = k_{n,d} e^{in\theta_d}. \quad (27)$$

The contribution of this subspace to the dot-product attention is the real part of $q'_{m,d}(k'_{n,d})^*$:

$$\text{atten}_d(m, n) = \text{Re}[q'_{m,d}(k'_{n,d})^*] = \text{Re}[q_{m,d}k_{n,d}^* e^{i\theta_d(m-n)}]. \quad (28)$$

Writing $q_{m,d}k_{n,d}^*$ in polar form as $q_{m,d}k_{n,d}^* = A_d(m, n)e^{i\varphi_d(m,n)}$ with $A_d(m, n) \geq 0$ and $\varphi_d(m, n) \in \mathbb{R}$, we obtain

$$\begin{aligned} \text{atten}_d(m, n) &= \text{Re}[A_d(m, n)e^{i(\theta_d(m-n) + \varphi_d(m,n))}] \\ &= A_d(m, n) \cos(\theta_d(m - n) + \varphi_d(m, n)), \end{aligned} \quad (29)$$

which shows that $\text{atten}_d(m, n)$ is proportional to a cosine function of the relative distance $(m - n)$, with angular frequency θ_d . The periodicity with period $2\pi/\theta_d$ follows immediately from the periodicity of the cosine function. \square

D.4.2. DETAILS OF DRoPE

The initial RoPE frequencies θ_d typically exhibit a wide numerical range. For instance, in our setting $\theta_0 = 1.0$ ($d = 0$), while $\theta_{31} \approx 1.33 \times 10^{-4}$ ($d = 31$, corresponding to $D_h/2 - 1$ and $D_h = 64$). Directly applying affine modulation to these values could lead to numerical instability or disproportionate adjustments due to the vast scale differences.

To address this and ensure stable and effective modulation across the entire range of base frequencies, our DRoPE performs the adaptation in log-space. The layer-specific modulation parameters, $\gamma_d^{(l)}$ and $\beta_d^{(l)}$, predicted by the Multilayer Perceptron (MLP) for layer l following Algorithm 1, are applied to the log-transformed base frequencies $\log \theta_d$ via an element-wise affine transformation as

$$\log \theta'_{\text{inst},d} = \gamma_d^{(l)} \odot \log \theta_d + \beta_d^{(l)}, \quad (30)$$

where $\log \theta'_{\text{inst},d}$ represents the modulated log-frequencies for layer l and dimension pair d . Then, these modulated log-frequencies are transformed back to their original scale by exponentiation to obtain the adaptive rotation frequencies $\theta'_{\text{inst},d}$ used in the DRoPE calculation for layer l as

$$\theta'_{\text{inst},d} = \exp(\log \theta'_{\text{inst},d}). \quad (31)$$

Algorithm 1 Generating Instance Adaptive Parameters ($\gamma^{(l)}, \beta^{(l)}$)

Require: Time series instance $X \in \mathbb{R}^{B \times L}$, mask $M \in \{0, 1\}^{B \times L}$, batch size B , sequence length L , FFT feature dimension w , MLP network f_{MLP}

Ensure: Adaptive parameters $\gamma^{(l)} \in \mathbb{R}^{B \times D_n/2}$, $\beta^{(l)} \in \mathbb{R}^{B \times D_n/2}$

- 1: $X_{\text{masked}} \leftarrow X \odot M$ {Apply mask (element-wise product)}
 - 2: $F_{\text{result}} \leftarrow \text{RFFT}(X_{\text{masked}})$, $F_{\text{result}} \in \mathbb{R}^{B \times (\frac{L}{2} + 1)}$ {Real FFT along sequence dim}
 - 3: $F_{\text{amp}} \leftarrow |F_{\text{result}}|$, $F_{\text{amp}} \in \mathbb{R}^{B \times (\frac{L}{2} + 1)}$ {Amplitude spectrum}
 - 4: $X_{\text{FFT}} \leftarrow F_{\text{amp}}[\dots, : w]$, $X_{\text{FFT}} \in \mathbb{R}^{B \times w}$ {Truncate low frequency}
 - 5: $X'_{\text{FFT}} \leftarrow \text{LayerNorm}_{\text{FFT}}(X_{\text{FFT}})$ {Normalize FFT features}
 - 6: $\gamma^{(l)}, \beta^{(l)} \leftarrow f_{\text{MLP}}(X'_{\text{FFT}})$ {Get instance-specific parameters}
 - 7: **return** $\gamma^{(l)}, \beta^{(l)}$
-

D.4.3. INTERPRETATION OF DROPE

From the theorem D.1, the base RoPE parameters $\{\theta_d\}_{d=0}^{D_n/2-1}$ define a fixed bank of sinusoidal kernels over relative positions. Each θ_d controls the frequency of one cosine kernel. This fixed frequencies works reasonably well when sequences share a homogeneous notion of temporal scale, but it can become suboptimal for a TSFM that must handle highly heterogeneous sampling intervals and spectral patterns across domains.

DRoPE addresses this by making these frequencies instance-adaptive. The FFT-based module in Algorithm 1 extracts simple spectral statistics X'_{FFT} from each input sequence and maps them, via an MLP, to instance- and layer-specific parameters $\gamma_d^{(l)}$ and $\beta_d^{(l)}$. These parameters modulate the base frequencies in log-space:

$$\log \theta'_{\text{inst},d} = \gamma_d^{(l)} \odot \log \theta_d + \beta_d^{(l)}, \quad \theta'_{\text{inst},d} = \exp(\log \theta'_{\text{inst},d}), \quad (32)$$

yielding an adapted frequency grid $\{\theta_d^{(l)}\}$ for each layer and sequence.

Intuitively, this log-space affine transformation stretches or compresses the original RoPE frequency grid in a sequence-dependent way, while preserving the relative-position nature of RoPE. The resulting $\theta'_{\text{inst},d}$ still define sinusoidal kernels over relative lags, but their effective frequencies are now gently steered by the spectrum of the current input. Crucially, DRoPE does not aim to recover a single true period for each series; real-world time series are often multi-periodic and non-stationary. Instead, we interpret $\{\theta'_{\text{inst},d}\}$ as a sequence-dependent frequency profile that shapes how attention depends on relative lags, providing a more flexible and data-driven positional bias than fixed RoPE.

E. Additional Details of Experiment Setting

E.1. Pre-training Datasets

We trained KAIROS on the Predictability-Stratified Time Series (PreSTS) corpus, which consists of over 300B real-world time series observations from Chronos (Ansari et al., 2024) and Moirai (Woo et al., 2024) in conjunction with 15B synthetic time points. Following (Das et al., 2024), the training loader samples 80% real data and 20% synthetic data.

Real-world data. The real-world datasets were stratified into five tiers based on their predictability. This hierarchical structure dictates the sampling probability during model training, assigning a higher likelihood of selection to datasets with greater predictability. Such a strategy ensures that the model is preferentially trained on high-quality data while preserving its capacity to predict corner cases. Specifically, Tier 1 comprises datasets characterized by pronounced periodicity and trends with low noise. Tier 2 contains datasets with similarly distinct patterns but high noise, whereas Tier 3 includes those with subtle trends and considerable noise. The remaining datasets were classified into Tiers 4 and 5, based on a composite assessment of their size and pattern regularity. The specific details of these datasets, categorized by their respective sampling frequencies, are presented in Tables 6-9.

Synthetic data. We build a synthetic data generator that produces two distinct types of time series, each with a length of 4096. The first type consists of composite series, created by the additive combination of seasonal, trend, and noise components. For seasonality, we sample one or two components, where the primary period is drawn from $\{24, 48, 288,$

360}, and a potential second period is a fixed seven-fold multiple of the first; the seasonal patterns manifest as either spike trains or smooth non-sinusoidal templates generated via interpolation. An optional trend is chosen from linear, exponential, or an ARIMA-like process derived from cumulating a stationary ARMA model’s output. High-probability white Gaussian noise is also added, with each series guaranteed to contain at least one seasonal or trend component and all magnitudes bounded for stability. The generation process for these composite series is formally detailed in Algorithm 2. Complementing these are idealized industrial signals, which simulate perfectly regular machine cycles. These feature a constant baseline with repeating events like trapezoidal spikes or inverted-U shaped dips, where the period, amplitude, and width of the events remain fixed across the entire series with no random jitter, as outlined in Algorithm 3. Synthetic dataset cases are provided in Appendix H.1.

Distribution Analysis. To investigate whether the synthetic dataset supplements distributions absent in the real-world data, we adopted the statistical methodology of Toto (Cohen et al., 2025). We employed the ARCH-LM Statistic and Spectral Entropy to quantify time-varying volatility and information density (complexity), respectively. These metrics align closely with the design motivation for the Mixture-of-Size Encoding and DRoPE components of KAIROS. As illustrated in Figures 6 (a) and (b), we observed that a significant portion of the real-world dataset exhibits ARCH-LM Statistic values approaching zero and Spectral Entropy values nearing one, indicating high time-varying volatility and complexity. In contrast, the synthetic dataset exhibits the opposite characteristics, exposing the model during training to time series with more constant volatility and greater regularity. This exposure enhances the model’s generalization capabilities. Furthermore, we statistically compared the periodicity of the real-world and synthetic datasets by plotting their respective Cumulative Distribution Functions (CDFs). As shown in Figure 6 (c), the dominant periods in the real-world dataset are heavily concentrated. This can cause the model to overfit to these specific periodicities and fail to learn generalizable periodic patterns. Conversely, the synthetic dataset presents a significantly smoother distribution of periods, enabling the model to generalize effectively across arbitrary periodicities. Consequently, the synthetic dataset effectively mitigates these biases present in the real-world data, thereby exposing the model to a more comprehensive and diverse set of distributions.

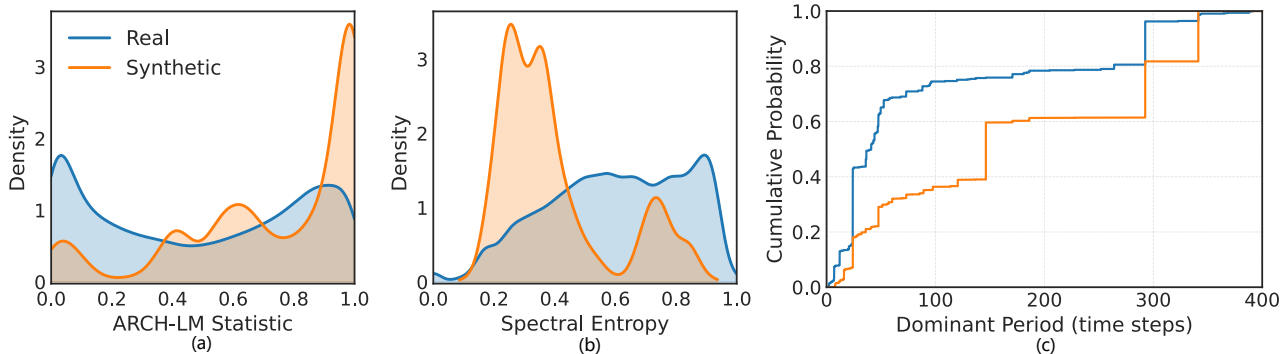


Figure 6. Comparison of real and synthetic datasets across (a) ARCH-LM statistic, (b) spectral entropy, and (c) dominant period distributions, illustrating complementary volatility, complexity, and periodicity characteristics.

E.2. Evaluation Datasets

We select datasets from diverse domains and with varying sampling frequencies as evaluation datasets. The details are summarized in Table 10. For the evaluation on the TSLib benchmark, the datasets were split into training, validation, and test sets. The split for the ETT and Weather datasets follows the configuration adopted by iTransformer (Liu et al., 2023). All other datasets use a 70%/10%/20% ratio for the training, validation, and test sets, respectively.

E.3. Evaluation Length Selection

In this section, we provide further details regarding the selection of historical sequence lengths for the various models evaluated in the TSLib benchmark, supplementing the discussion in Section 4.1.1.

To accommodate diverse application scenarios, an increasing number of TSFMs (Liu et al., 2025; Das et al., 2024; Liu et al., 2024c; Woo et al., 2024) have devoted attention to predicting over long contexts. Consequently, we evaluate KAIROS and other TSFMs under a long-context setting. Specifically, we adopt a context length of 2048 time steps and examine four prediction horizons, which are {96,192,336,720}. For TSFMs incapable of processing this context length, we instead

Table 6. Detailed descriptions of second-level, minute-level, and hourly datasets.

Dataset	Domain	Frequency	# Time Series	# Time points
Wind Power	Energy	4S	1	7,397,147
Residential Load Power	Energy	T	813	437,983,677
Residential PV Power	Energy	T	699	376,016,850
Los-Loop	Transport	5T	207	7,094,304
PEMS03	Transport	5T	358	9,382,464
PEMS04	Transport	5T	921	15,649,632
PEMS07	Transport	5T	883	24,921,792
PEMS08	Transport	5T	510	9,106,560
PEMS Bay	Transport	5T	325	16,941,600
Alibaba Cluster Trace 2018	CloudOps	5T	116,818	190,385,060
Azure VM Traces 2017	CloudOps	5T	159,472	885,522,908
Borg Cluster Data 2011	CloudOps	5T	286,772	1,075,105,708
LargeST	Transport	5T	42,333	4,452,510,528
KDD Cup 2022	Energy	10T	134	4,727,519
HZMetro	Transport	15T	160	380,320
Q-Traffic	Transport	15T	45,148	264,386,688
SHMetro	Transport	15T	576	5,073,984
Beijing Subway	Transport	30T	552	867,744
Elecdemand	Energy	30T	1	17,520
Australian Electricity Demand	Energy	30T	5	1,155,264
London Smart Meters	Energy	30T	5,560	166,528,896
Taxi	Transport	30T	2428	3,589,798
BDG-2 Bear	Energy	H	91	1,482,312
BDG-2 Fox	Energy	H	135	2,324,568
BDG-2 Panther	Energy	H	105	919,800
BDG-2 Rat	Energy	H	280	4,728,288
Borealis	Energy	H	15	83,269
BDG-2 Bull	Energy	H	41	719,304
China Air Quality	Nature	H	2,622	34,435,404
BDG-2 Cockatoo	Energy	H	1	17,544
Covid19 Energy	Energy	H	1	31,912
ELF	Energy	H	1	21,792
GEF12	Energy	H	20	788,280
GEF14	Energy	H	1	17,520
GEF17	Energy	H	8	140,352
BDG-2 Hog	Energy	H	24	421,056
IDEAL	Energy	H	217	1,255,253
Low Carbon London	Energy	H	713	9,543,553
Oikolab Weather	Climate	H	8	800,456
PDB	Energy	H	1	17,520
Sceaux	Energy	H	1	34,223
SMART	Energy	H	5	95,709
Spanish Energy and Weather	Energy	H	1	35,064
ERCOT Load	Energy	H	8	1,238,976
Mexico City Bikes	Transport	H	494	38,687,004
Beijing Air Quality	Nature	H	132	4,628,448
Pedestrian Counts	Transport	H	66	3,132,346
Rideshare	Transport	H	2,304	859,392
Traffic	Transport	H	862	15,122,928
Taxi (Hourly)	Transport	H	2,428	1,794,292
Uber TLC (Hourly)	Transport	H	262	1,138,128
Wind Farms (Hourly)	Energy	H	337	2,869,414
Weatherbench (Hourly)	Nature	H	225,280	78,992,150,528
Buildings900K	Energy	H	1,795,256	15,728,237,816
ERA5	Climate	H	11,059,200	96,613,171,200
CMIP6	Climate	6H	14,327,808	104,592,998,400

Table 7. Detailed descriptions of daily datasets.

Dataset	Domain	Frequency	# Time Series	# Time points
Bitcoin	Econ/Fin	D	18	81,918
Covid Mobility	Transport	D	362	148,602
Extended Web Traffic	Web	D	145,063	370,926,091
Favorita Sales	Sales	D	111,840	139,179,538
Favorita Transactions	Sales	D	54	84,408
Subseasonal	Climate	D	3,448	56,788,560
Subseasonal Precipitation	Climate	D	862	9,760,426
Sunspot	Nature	D	1	73,894
Vehicle Trips	Transport	D	329	32,512
Wiki-Rolling	Web	D	47,675	40,619,100
Dominick	Retail	D	100,014	29,652,492
M5	Sales	D	30,490	47,649,940
Monash Weather	Climate	D	3,010	43,032,000
NN5 Daily	Econ/Fin	D	111	87,801
Uber TLC Daily	Transport	D	262	47,422
Weatherbench (Daily)	Nature	D	225,280	3,291,336,704
Wiki Daily (100k)	Web	D	100,000	274,100,000
Wind Farms (Daily)	Energy	D	337	119,549
Exchange Rate	Finance	D	8	60,704

Table 8. Detailed descriptions of weekly datasets.

Dataset	Domain	Frequency	# Time Series	# Time points
CDC Fluview ILINet	Healthcare	W	375	319,515
CDC Fluview WHO NREVSS	Healthcare	W	296	167,040
Kaggle Web Traffic Weekly	Web	W	145,063	16,537,182
Project Tycho	Healthcare	W	1,258	1,377,707
Traffic Weekly	Transport	W	862	82,752
NN5 Weekly	Econ/Fin	W	111	12,543
Weatherbench (Weekly)	Nature	W	225,280	470,159,360

Table 9. Detailed descriptions of monthly, quarterly, and yearly datasets.

Dataset	Domain	Frequency	# Time Series	# Time points
GoDaddy	Econ/Fin	M	6,270	257,070
CIF 2016	Econ/Fin	M	72	7,108
FRED MD	Econ/Fin	M	107	77,896
M1 Monthly	Econ/Fin	M	617	55,998
M3 Monthly	Econ/Fin	M	1,428	167,562
Tourism Monthly	Econ/Fin	M	366	109,280
M3 Other	Econ/Fin	Q	174	11,933
M1 Quarterly	Econ/Fin	Q	203	9,944
M3 Quarterly	Econ/Fin	Q	756	37,004
Tourism Quarterly	Econ/Fin	Q	427	42,544
M1 Yearly	Econ/Fin	Y	181	4,515
M3 Yearly	Econ/Fin	Y	645	18,319
Tourism Yearly	Econ/Fin	Y	518	12,757

Algorithm 2 Composite Time Series Generation

Require: Time series length $L = 4096$, Primary period set $\mathcal{P}_1 = \{24, 48, 288, 360\}$, Harmonic multiplier $n = 7$, Trend types $\mathcal{T}_{\text{types}} = \{\text{linear, exp, ARMA}\}$, Seasonal patterns $\mathcal{S}_{\text{patterns}} = \{\text{spike, interpolated segment}\}$.

Ensure: A synthetic time series $x_{1:L}$.

```

1:  $x, s, t, n \leftarrow \mathbf{0}_{1:L}$  {Initialize total series and components (seasonal, trend, noise)}
2: Sample flags  $f_s, f_t, f_n$  {Determine component inclusion, ensuring  $f_s \vee f_t$  is true}
3: if  $f_s$  is true then
4:    $k \sim \text{Bernoulli}(0.2)$  { $k = 1$  for double period (20% prob),  $k = 0$  for single}
5:    $p_1 \sim \mathcal{U}(\mathcal{P}_1)$  {Sample primary period}
6:    $\mathcal{P}_{\text{active}} \leftarrow \{p_1\}$ 
7:   if  $k = 1$  then
8:      $\mathcal{P}_{\text{active}} \leftarrow \mathcal{P}_{\text{active}} \cup \{n \cdot p_1\}$ 
9:   end if
10:  for all  $p$  in  $\mathcal{P}_{\text{active}}$  do
11:     $a \sim \mathcal{U}(1.0, 3.0)$  {Sample amplitude for this component}
12:     $pattern \sim \mathcal{U}(\mathcal{S}_{\text{patterns}})$ 
13:     $c \leftarrow \text{GeneratePattern}(pattern, p, a)$  {Create a single cycle of the pattern}
14:     $s \leftarrow s + \text{Tile}(c, L)$  {Tile the cycle to length  $L$  and add to seasonal component}
15:  end for
16: end if
17: if  $f_t$  is true then
18:    $type \sim \mathcal{U}(\mathcal{T}_{\text{types}})$ 
19:    $t \leftarrow \text{GenerateTrend}(type, L)$ 
20: if  $f_s$  is true then
21:    $\lambda \sim \mathcal{U}(0.1, 0.3)$  {Reduce trend strength when seasonality is present}
22:    $t \leftarrow \lambda \cdot t$ 
23: end if
24: end if
25: if  $f_n$  is true then
26:    $\sigma_n \sim \mathcal{U}(0.01, 0.1)$ 
27:    $n \sim \mathcal{N}(\mathbf{0}, \sigma_n^2 \mathbf{I})$  {Generate white Gaussian noise}
28: end if
29:  $x \leftarrow s + t + n$ 
30: return  $x_{1:L}$ 

```

Table 10. Detailed descriptions of evaluation datasets.

Dataset	Domain	Frequency	# Time Series	# Target	# Time points
ETTh1	Energy	H	1	7	17,420
ETTh2	Energy	H	1	7	17,420
ETTm1	Energy	15T	1	7	69,680
ETTm2	Energy	15T	1	7	69,680
Weather	Nature	10T	1	21	52,696
Saugeen (D)	Nature	D	1	1	23,741
Saugeen (W)	Nature	W	1	1	3,391

Algorithm 3 Idealized Industrial Signal Generation

Require: Time series length $L = 4096$, Pattern types $\mathcal{P}_{\text{types}} = \{\text{inverted_u, spikes}\}$.
Ensure: A synthetic time series $\mathbf{x}_{1:L}$.

- 1: $type \sim \mathcal{U}(\mathcal{P}_{\text{types}})$
- 2: $(b, p, a, w, \sigma_n) \leftarrow \text{SampleParams}(type)$ {Sample baseline, period, amplitude, width, noise}
- 3: $\mathbf{x}_{1:L} \leftarrow b$ {Initialize series with baseline value}
- 4: $\mathbf{e} \leftarrow \text{TrapezoidShape}(w, a)$ {Create the event shape of width w and amplitude a }
- 5: **if** $type = \text{inverted_u}$ **then**
- 6: $sign \leftarrow -1$
- 7: **else**
- 8: $sign \leftarrow +1$
- 9: **end if**
- 10: **for all** $i \leftarrow 0, p, 2p, \dots$ up to $L - 1$ **do**
- 11: $start \leftarrow i, end \leftarrow \min(i + w, L)$
- 12: $\mathbf{x}_{start:end} \leftarrow \mathbf{x}_{start:end} + sign \cdot \mathbf{e}_{1:end-start}$ {Add or subtract event shape at periodic intervals}
- 13: **end for**
- 14: **if** $\sigma_n > 0$ **then**
- 15: $\mathbf{x} \leftarrow \mathbf{x} + \mathcal{N}(\mathbf{0}, \sigma_n^2 \mathbf{I})$ {Add global Gaussian noise}
- 16: **end if**
- 17: **return** $\mathbf{x}_{1:L}$

employ the context length at which each model achieves its best performance.

For the full-shot deep learning baselines, **a hyperparameter search was conducted independently for each dataset to ensure a fair evaluation**. We compared the performance of each model using the context length from its original publication against a length of 2048, selecting the superior of the two. To be specific, lengths of 96 and 2048 were compared for DLinear (Zeng et al., 2022), iTransformer (Liu et al., 2023), TimesNet (Wu et al., 2022), and Patchformer, while lengths of 336, 512, and 2048 were compared for PatchTST (Nie et al., 2023).

The definitive context lengths adopted for each model are systematically tabulated in Table 11.

Table 11. Context Lengths for Models on the TSLib Benchmark.

Method	DLinear	iTrans.	TimesNet	PatchTST	Path.	Chronos	Moirai	TimesFM-2.0	Timer-XL	TTM _a	ChronosBolt	KAIROS
Context length	{96, 2048}	{96, 2048}	{96, 2048}	{336, 512, 2048}	{96, 2048}	512	2048	2048	2048	1536	2048	2048

E.4. Details of DRoPE Analysis

In this section, we explain in more detail the setting of the DRoPE analysis experiment discussed in Section 4.4.2. To more definitively ascertain whether these instance-specific modulations truly capture and leverage beneficial positional information derived from an instance’s FFT features, we designed a series of “shuffle” experiments. These experiments function as a form of causal intervention analysis. The underlying hypothesis is: if the instance-derived θ_{inst} modulations are crucial for DRoPE’s performance, then disrupting this linkage by applying θ_{inst} modulations from one instance to another (shuffling) should lead to a noticeable degradation in forecasting accuracy.

The details of each group in the experiment are as follows:

- DRoPE: Our proposed method, where each time series instance utilizes its own FFT-derived features to independently modulate its RoPE θ_{inst} parameters at each layer.
- Intra-Dataset Shuffle: During inference, the learned layer-specific θ_{inst} modulation parameters $(\gamma^{(l)}, \beta^{(l)})$ are randomly permuted among instances within the same batch and originating from the same dataset. The modulated θ_{inst} are always shuffled in the same layer.
- Inter-Dataset Shuffle: For instances of a target dataset, layer-specific θ_{inst} modulation parameters $(\gamma^{(l)}, \beta^{(l)})$ are randomly

sampled from a pre-computed collection derived from a different source dataset and applied to instances of the target dataset. This process also ensures layer-wise correspondence of the applied modulations.

- **Fixed RoPE:** We use the fully trained DRoPE model but disable its instance-adaptive modulation during inference. Specifically, the prediction of $\gamma^{(l)}$ and $\beta^{(l)}$ is bypassed, and all instances revert to using the initial RoPE θ across all layers. This approach keeps the base model architecture and other learned weights identical to DRoPE, isolating the effect of the modulation.

By comparing DRoPE’s performance against these shuffled and fixed θ configurations, we can better attribute performance gains or losses to the effectiveness of the instance-adaptive θ_{inst} modulation process.

F. Full Evaluation Results

In this section, we present the detailed results in Section 4.2. Table 12 presents the full results of the zero-shot forecasting experiments conducted at each forecast horizon. For Time-MoE, we report the results as presented in the original paper (Shi et al., 2024).

G. Calculation of information density

In this section, we present the formula for the information density illustrated in Figure 1(b). To effectively characterize and compare different time series datasets, we introduce a method to quantify their information density and the variation of this density over time. For this, similar to TimeMixer (Wang et al., 2024a), we utilize spectral entropy, a metric that measures the complexity and compressibility of a signal. In this context, a signal with low spectral entropy, such as one with a few dominant periodic components, is considered to have low information density due to its redundant and predictable nature. Conversely, a signal with high spectral entropy, resembling white noise, has its power spread broadly across the frequency spectrum, indicating a high degree of randomness and thus a higher information density.

Given the observations $\mathbf{x}_{1:T} = (x_1, \dots, x_T) \in \mathbb{R}^T$ of a specific dataset, we analyze the time series using a sliding window approach. The series is segmented into N windows, \mathbf{w}_i , each of size M with a step size of S . In our analysis, we use a non-overlapping configuration where both the window size and the step size are set to 128 (i.e., $M = 128, S = 128$). The total number of windows is $N = \lfloor (T - M)/S \rfloor + 1$. To mitigate spectral leakage from windowing, we apply a Hamming window to each segment \mathbf{w}_i :

$$h[n] = 0.5 - 0.5 \cos\left(\frac{2\pi n}{M-1}\right), \quad 0 \leq n \leq M-1. \quad (33)$$

For each resulting windowed segment $\mathbf{w}'_i = \mathbf{w}_i \cdot h$, we compute its normalized power spectral density, $p_i[k]$, which describes how the signal’s power is distributed over different frequencies. The spectral entropy for the i -th window, $H_{SE}(\mathbf{w}_i)$, is then calculated using the Shannon entropy formula:

$$H_{SE}(\mathbf{w}_i) = - \sum_{k=0}^{M-1} p_i[k] \log_2(p_i[k]). \quad (34)$$

This process yields a sequence of entropy values, $(H_{SE}(\mathbf{w}_1), \dots, H_{SE}(\mathbf{w}_N))$, where each value represents the localized information density of its corresponding time segment.

To obtain a holistic view of the dataset’s characteristics, we compute two key statistics from this entropy sequence.

First, the mean spectral entropy (μ_{SE}) serves as a measure of the average information density of the entire dataset. A higher μ_{SE} suggests that the dataset, on average, contains more complex and less predictable patterns. This allows for a direct comparison of the overall information content between different datasets.

$$\mu_{SE} = \frac{1}{N} \sum_{i=1}^N H_{SE}(\mathbf{w}_i). \quad (35)$$

Second, the standard deviation of spectral entropy (σ_{SE}) quantifies the variability of information density within the dataset. A small σ_{SE} indicates that the dataset is stationary in its complexity, with a consistent level of information density throughout.

Table 12. Full results of zero-shot forecasting experiments.

Method	Metric	ETh1				ETh2				ETIm1				ETIm2				Weather				Saugent(D)				Saugent(W)				Total J [†]	AVG							
		96	192	336	720	96	192	336	720	96	192	336	720	96	192	336	720	96	192	336	720	96	192	336	720	96	192	336	720									
DLinear	MSE	0.377	0.416	0.446	0.482	0.430	0.280	0.398	0.505	0.796	0.495	0.312	0.354	0.401	0.364	0.401	0.354	0.174	0.228	0.287	0.396	0.271	0.174	0.214	0.256	0.309	0.238	0.829	0.832	0.826	0.858	0.836	0.820	0.849	0.781	0.817	0.480	
	MAE	0.391	0.416	0.440	0.454	0.495	0.436	0.388	0.434	0.495	0.359	0.379	0.392	0.415	0.385	0.272	0.312	0.355	0.428	0.342	0.238	0.272	0.304	0.346	0.290	0.502	0.503	0.502	0.503	0.506	0.513	0.506	0.509	0.571	0.551	0.564	0.424	
	MAE	0.383	0.421	0.478	0.470	0.443	0.382	0.367	0.402	0.406	0.364	0.327	0.363	0.390	0.424	0.376	0.376	0.369	0.398	0.428	0.383	0.383	0.171	0.218	0.258	0.357	0.256	0.778	0.795	0.800	0.839	0.988	1.041	1.007	1.012	0.901	0.501	
tTransformer	MSE	0.396	0.429	0.449	0.469	0.436	0.344	0.392	0.422	0.433	0.398	0.355	0.381	0.411	0.442	0.397	0.355	0.381	0.411	0.442	0.397	0.210	0.256	0.299	0.351	0.279	0.457	0.482	0.490	0.473	0.626	0.640	0.642	0.636	0.423	0.423	-	
	MAE	0.408	0.456	0.508	0.567	0.485	0.315	0.435	0.481	0.455	0.422	0.358	0.428	0.494	0.450	0.458	0.428	0.458	0.450	0.458	0.428	0.222	0.265	0.304	0.352	0.286	0.546	0.561	0.534	0.531	0.543	0.517	0.494	0.501	0.504	0.423	-	
	MAE	0.432	0.451	0.496	0.521	0.469	0.359	0.422	0.456	0.461	0.425	0.373	0.412	0.447	0.480	0.428	0.385	0.403	0.407	0.438	0.382	0.222	0.265	0.304	0.352	0.286	0.546	0.561	0.534	0.531	0.543	0.517	0.494	0.501	0.504	0.423	-	
PatchTST	MSE	0.436	0.416	0.443	0.466	0.427	0.280	0.351	0.388	0.424	0.361	0.278	0.327	0.363	0.414	0.346	0.162	0.221	0.270	0.369	0.256	0.149	0.195	0.254	0.346	0.236	0.827	0.83	0.819	0.848	0.831	0.849	0.847	0.781	0.826	0.456	-	
	MAE	0.403	0.426	0.444	0.474	0.437	0.349	0.393	0.420	0.445	0.402	0.330	0.361	0.388	0.423	0.376	0.249	0.291	0.323	0.386	0.354	0.275	0.474	0.482	0.488	0.491	0.484	0.545	0.526	0.500	0.524	0.397	-	0.397	-			
	MAE	0.405	0.466	0.506	0.494	0.468	0.276	0.365	0.420	0.429	0.373	0.302	0.356	0.395	0.463	0.379	0.162	0.225	0.290	0.414	0.273	0.152	0.200	0.258	0.341	0.238	1.168	1.266	1.142	1.149	1.181	0.932	0.949	0.877	0.919	0.533	-	
Pathformer	MSE	0.403	0.466	0.506	0.494	0.468	0.276	0.365	0.420	0.429	0.373	0.302	0.356	0.395	0.463	0.379	0.162	0.225	0.290	0.414	0.273	0.152	0.200	0.258	0.341	0.238	1.168	1.266	1.142	1.149	1.181	0.932	0.949	0.877	0.919	0.533	-	
	MAE	0.398	0.427	0.447	0.463	0.434	0.334	0.386	0.428	0.443	0.398	0.325	0.361	0.388	0.429	0.376	0.244	0.288	0.333	0.403	0.317	0.192	0.237	0.281	0.335	0.261	0.501	0.535	0.502	0.499	0.511	0.532	0.532	0.533	0.532	0.332	0.399	-
	MAE	0.516	0.599	0.613	0.603	0.583	0.304	0.407	0.427	0.450	0.397	0.304	0.601	0.667	0.728	0.625	0.207	0.277	0.343	0.468	0.324	0.209	0.267	0.328	0.397	0.300	1.108	1.142	1.105	1.145	1.125	1.183	1.227	1.166	1.192	0.629	0.426	0
Chronos _s	MSE	0.416	0.464	0.487	0.512	0.470	0.347	0.401	0.428	0.457	0.408	0.398	0.457	0.498	0.538	0.473	0.277	0.323	0.364	0.437	0.350	0.213	0.263	0.307	0.386	0.285	0.477	0.503	0.506	0.512	0.500	0.520	0.524	0.526	0.523	0.426	0	
	MAE	0.526	0.585	0.593	0.608	0.578	0.322	0.411	0.440	0.443	0.404	0.422	0.523	0.600	0.686	0.558	0.206	0.272	0.329	0.436	0.311	0.184	0.241	0.296	0.375	0.274	1.172	1.224	1.202	1.249	1.212	1.166	1.222	1.157	1.182	0.626	0.415	0
	MAE	0.413	0.447	0.461	0.491	0.453	0.343	0.392	0.422	0.440	0.399	0.374	0.434	0.477	0.520	0.451	0.270	0.316	0.354	0.420	0.340	0.206	0.256	0.298	0.353	0.274	0.473	0.505	0.502	0.505	0.496	0.515	0.517	0.508	0.513	0.415	0	
Chronos _l	MSE	0.493	0.601	0.636	0.653	0.596	0.328	0.434	0.480	0.522	0.442	0.452	0.536	0.613	0.671	0.568	0.203	0.268	0.316	0.424	0.303	0.195	0.254	0.311	0.395	0.285	1.178	1.229	1.194	1.232	1.208	1.213	1.269	1.241	1.241	0.642	0	
	MAE	0.400	0.449	0.475	0.503	0.457	0.348	0.407	0.448	0.482	0.421	0.379	0.430	0.470	0.512	0.448	0.263	0.309	0.342	0.408	0.331	0.211	0.264	0.305	0.360	0.285	0.481	0.508	0.499	0.499	0.497	0.523	0.534	0.534	0.534	0.420	0	
	MAE	0.395	0.430	0.445	0.430	0.425	0.274	0.341	0.364	0.378	0.339	0.363	0.385	0.410	0.450	0.402	0.192	0.258	0.307	0.391	0.287	0.160	0.207	0.258	0.327	0.238	1.083	1.112	1.085	1.105	1.096	1.272	1.284	1.177	1.244	0.551	4	
Motrials _s	MSE	0.404	0.427	0.436	0.445	0.428	0.324	0.369	0.386	0.405	0.371	0.360	0.379	0.399	0.422	0.390	0.263	0.308	0.340	0.397	0.327	0.194	0.238	0.275	0.324	0.258	0.479	0.493	0.491	0.493	0.489	0.560	0.562	0.555	0.552	0.397	4	
	MAE	0.429	0.494	0.531	0.544	0.500	0.275	0.347	0.379	0.388	0.347	0.459	0.482	0.518	0.479	0.194	0.251	0.292	0.354	0.273	0.170	0.218	0.270	0.344	0.251	1.129	1.175	1.142	1.177	1.156	1.208	1.243	1.171	1.207	0.579	2		
	MAE	0.412	0.447	0.467	0.501	0.457	0.319	0.365	0.388	0.408	0.370	0.385	0.400	0.415	0.435	0.409	0.266	0.306	0.333	0.375	0.320	0.203	0.249	0.288	0.339	0.270	0.472	0.495	0.485	0.485	0.484	0.557	0.550	0.538	0.548	0.403	2	
Motrials _l	MSE	0.464	0.523	0.546	0.549	0.521	0.298	0.403	0.464	0.530	0.424	0.522	0.541	0.563	0.611	0.559	0.195	0.257	0.308	0.395	0.289	0.170	0.222	0.277	0.361	0.258	1.102	1.140	1.102	1.122	1.117	1.213	1.252	1.179	1.215	0.604	0	
	MAE	0.433	0.470	0.486	0.511	0.475	0.346	0.412	0.448	0.498	0.426	0.401	0.423	0.442	0.463	0.433	0.267	0.311	0.342	0.395	0.329	0.203	0.253	0.293	0.347	0.274	0.464	0.486	0.484	0.486	0.480	0.541	0.543	0.534	0.539	0.418	0	
	MAE	0.424	0.444	0.443	0.438	0.437	0.256	0.328	0.366	0.391	0.335	0.362	0.410	0.429	0.470	0.418	0.175	0.239	0.294	0.369	0.269	-	-	-	-	-	1.099	1.106	1.088	1.088	1.088	1.277	1.448	3.971	2.332	-	0	
TimesFM-2.0	MSE	0.394	0.436	0.469	0.436	0.434	0.273	0.342	0.377	0.382	0.344	0.325	0.374	0.414	0.510	0.406	0.187	0.240	0.285	0.374	0.272	0.167	0.213	0.266	0.340	0.247	1.043	1.126	1.127	1.127	1.106	1.112	1.128	1.043	1.094	0.537	0	
	MAE	0.395	0.419	0.437	0.448	0.425	0.336	0.380	0.402	0.416	0.384	0.354	0.385	0.409	0.455	0.401	0.272	0.310	0.338	0.292	0.328	0.221	0.264	0.304	0.286	0.574	0.612	0.615	0.606	0.602	0.626	0.620	0.594	0.613	0.427	0		
	MAE	0.357	0.384	0.411	0.449	0.400	0.305	0.351	0.391	0.419	0.367	0.338	0.353	0.381	0.504	0.394	0.201	0.258	0.324	0.488	0.318	0.160	0.210	0.274	0.418	0.266	-	-	-	-	-	-	-	-	-	-	3	
Time-MoE _s	MSE	0.381	0.404	0.434	0.477	0.424	0.359	0.386	0.418	0.454	0.404	0.368	0.388	0.413	0.493	0.416	0.291	0.334	0.373	0.464	0.366	0.214	0.260	0.309	0.405	0.297	-	-	-	-	-	-	-	-	-	-	-	
	MAE	0.350	0.388	0.411	0.427	0.394	0.302	0.364	0.417	0.457	0.405	0.309	0.346	0.373	0.475	0.376	0.197	0.250	0.337	0.480	0.316	0.159	0.215	0.291	0.415	0.270	-	-	-	-	-	-	-	-	-	-	-	
	MAE	0.375	0.396	0.406	0.411	0.397	0.362	0.356	0.354	0.376	0.330	0.329	0.364	0.381	0.413	0.372	0.167	0.227	0.277	0.360	0.258	0.146	0.193	0.249	0.328	0.229	0.929	0.926	0.904	0.929	0.925	1.114	1.134	1.051	1.156	0.494	11	
TTM _s	MSE	0.397	0.415	0.424	0.441	0.419	0.334	0.378	0.400	0.421	0.383	0.350	0.374	0.390	0.410	0.381	0.284	0.296	0.329	0.382	0.135	0.197	0.242	0.289	0.265	0.511	0.518	0.523	0.541	0.523	0.628	0.608	0.621	0.408	0.488	-		
	MAE	0.405	0.475	0.514	0.516	0.478	0.255	0.339	0.388	0.400	0.346	0.309	0.																									

A large σ_{SE} , however, reveals a non-stationary character, signifying substantial fluctuations in the signal’s complexity and information content over time.

$$\sigma_{SE} = \sqrt{\frac{1}{N} \sum_{i=1}^N (H_{SE}(\mathbf{w}_i) - \mu_{SE})^2}. \quad (36)$$

Together, μ_{SE} and σ_{SE} provide a concise yet powerful summary of a dataset’s informational characteristics, enabling a quantitative assessment of its average complexity and internal dynamics.

H. Showcases

H.1. Showcases of Synthetic Data

Figure 7 showcases representative examples generated by the algorithm using the synthetic dataset. As detailed in Appendix E.1, the generated synthetic dataset is classified into two categories. The first is a composite type, formed from a combination of seasonal, trend, and noise components, which is designated Custom in the figures. The second consists of idealized industrial signals, designated Perfect periodic.

H.2. Showcases of KAIROS

We present several prediction examples generated by KAIROS during testing, as illustrated in Figure 8.

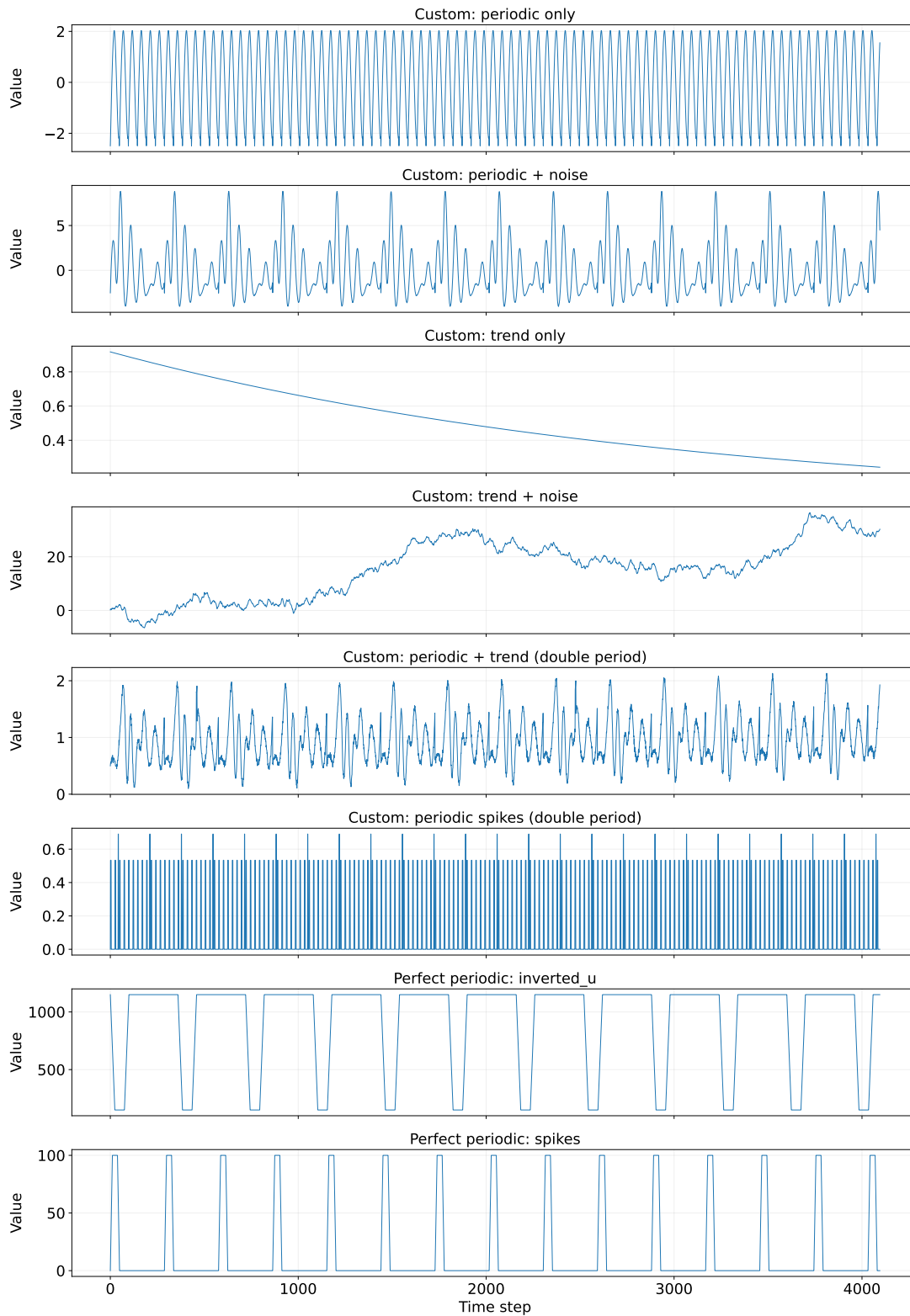


Figure 7. Several distinct case types are generated by the synthetic dataset algorithm. Specifically, the Custom designation refers to a composite signal type, which is systematically constructed by combining seasonal, trend, and noise components. Concurrently, the Perfect periodic designation denotes synthesized, idealized industrial signals.

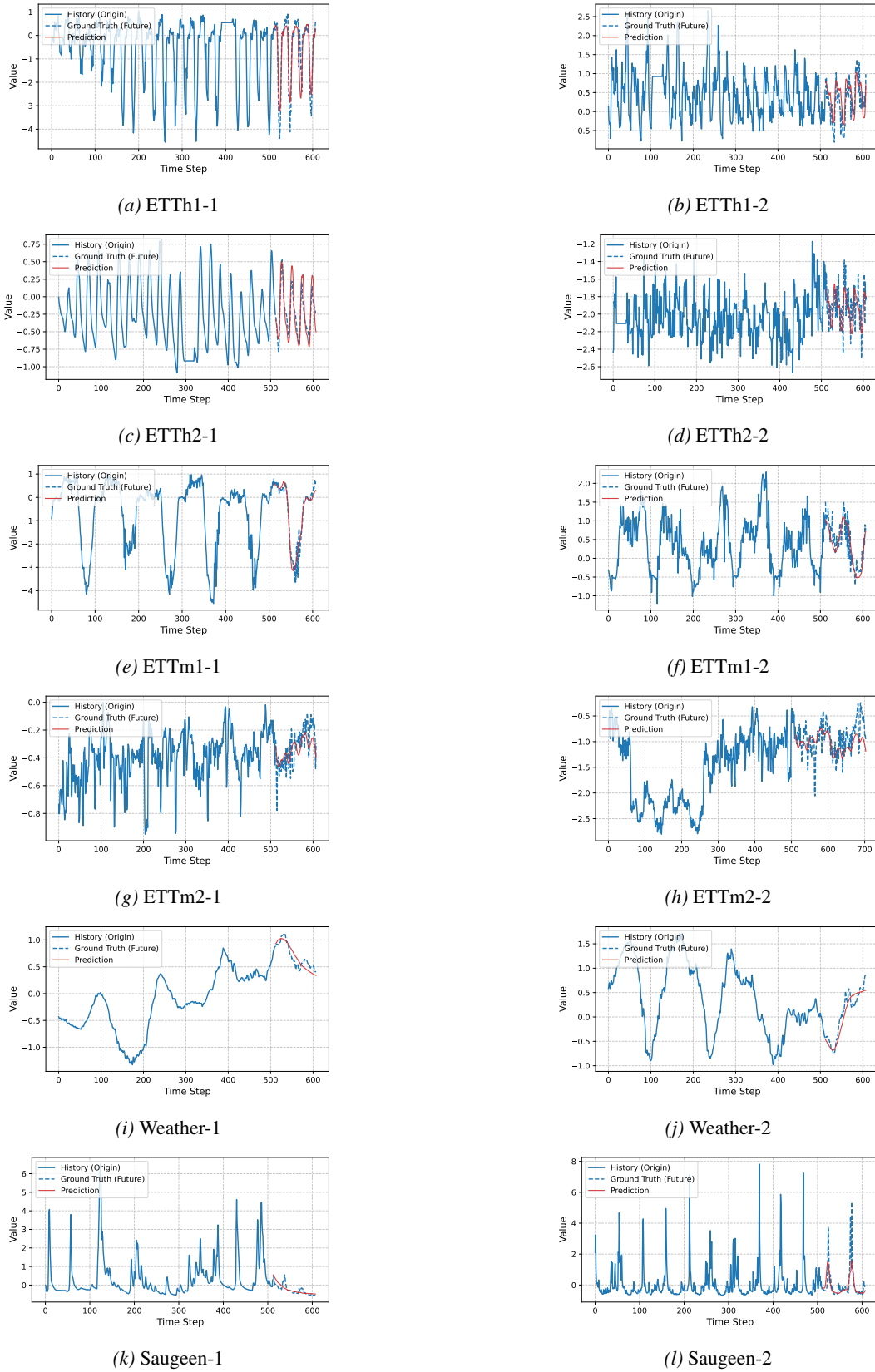


Figure 8. Example of forecasts from KAIROS_b on the test datasets used in experiments.